A Theoretical Study of the Tomographic Reconstruction of Magnetosheath X-ray Emissions

A. M. Jorgensen[1], R. Xu[2], T. Sun[2], Y. Huang[2], L. Li[3], L. Dai[2], C. Wang[2]

[1]New Mexico Institute of Mining and Technology, Socorro, NM, USA

[2]National Space Science Center, Chinese Academy of Sciences, Beijing, China

[3]Tsinghua University, Beijing, China

Key Points:

- Tomographic reconstruction of the magnetosheath with SMILE is possible
- High noise/low-count images can be used with regularization constraints
- Superposed epoch over a year works better than a single orbit

Corresponding author: =name=, =email address=

Abstract

We present an initial assessment of using tomography on single-spacecraft images to reconstruct 3D X-ray emissions from the Earth's magnetosheath. 3D structures in the Earth's magnetosphere have been studied using superposed epoch techniques with single-point single-spacecraft observations. They have yielded great insights, but some studies are observation starved, particularly for infrequent solar wind conditions. Global imaging data have provided more insight about these structures, but are 2D projections of 3D structures. We explore the use of tomographic reconstruction techniques to understand what can be extracted from global images from a single spacecraft. The Solar wind Magnetosphere Ionosphere Link Explorer (SMILE) mission, due to launch in 2024 on a 3-year mission, will carry a soft X-ray imager which will capture emissions from portions of the magnetosheath and upstream solar wind. We already demonstrated that the 3D shape of the magnetopause and the bow shock can be extracted from such images with suitable assumptions. The next step is to examine whether full 3D reconstructions of the emissions are possible. We explore the limited range of viewing angles, which affect the accuracy of the reconstructions and introduce artifacts in some cases, and the low count-rates in the images which introduce noise in the reconstructions which must be filtered out. Despite these limitations we show that it is possible to reconstruct some aspects of the magnetosheath global morphology using single-spacecraft soft X-ray imaging. Plans for similar missions which overlap with SMILE, open the possibility of multi-spacecraft tomography, to be addressed in a separate paper.

1 Introduction

Imaging has become an increasingly important tool for studying space plasma processes. Some of the earliest imaging was the imaging of auroras from the ground by Carl Størmer and associates for the purpose of triangulating their heights [e.g. *Størmer*, 1935]. Later work by Syun-Ichi Akasofu used auroral imaging from multiple sites on the ground to understand the development of the auroral substorm [e.g. *Akasofu*, 1964]. That was later followed by high-resolution imaging of the auroras from space by numerous spacecraft, including the UVI and VIS instruments on the Polar spacecraft launched in 1996 [e.g. *Brittnacher et al.*, 1997]. Imaging of emissions of large-scale plasma processes were done, for example imaging with Energetic Neutral Atom (ENA) [e.g. *Roelof et al.*, 1985; *Henderson et al.*, 1997; *C: son Brandt et al.*, 2002; *Vallat et al.*, 2004] to understand the ring

current and substorms [e.g. *Henderson et al.*, 1999; *Jorgensen et al.*, 2000]. Extreme Ultraviolet (EUV) radiation from the Sun scattered off of He^+ ions has been used to image the Earth's plasmasphere [e.g *Sandel et al.*, 2001; *He et al.*, 2016].

We have previously published on techniques for extracting the boundary shape of the magnetopause from soft X-ray images similar to those that will be produced by the Solar wind Magnetosphere Ionosphere Link Explorer (SMILE) mission [*Branduardi-Raymont et al.*, 2018; *Wang et al.*, 2017] Soft X-Ray Imager (SXI) instrument, by fitting a model for the boundary and the emissions distribution [*Jorgensen et al.*, 2019a,b]. Those methods fit 3D X-ray emissions and boundary models to individual X-ray images. Other methods include identification of the location of the boundaries directly in the images and using that to reconstruct those boundaries alone, from one or more images [*Collier and Connor*, 2018; *Sun et al.*]. Yet another option is the complete reconstruction of the 3D emissions based on multiple 2D images, analogous to the reconstruction techniques used in medical imaging. These techniques are collectively referred to as tomographic techniques. Tomographic techniques have previously been used in reconstructing the 3D shape of auroral formations [e.g. *Aso et al.*, 1998; *Gustavsson*, 1998]. In this paper we explore applying these tomographic techniques to the problem of imaging X-ray emissions under condition of a limited range of viewing angles.

In the following section, section 2, we provide a brief general introduction to tomographic techniques, and then discuss how we apply them to imaging of X-ray emissions. While medical imaging is usually carried out with specialized equipment which ensures a wide range of viewing geometries, imaging based on spacecraft observations will be constrained by the orbit of the spacecraft. In this paper we will focus on what is possible using the SMILE orbit and SXI camera and the most basic tomographic reconstruction techniques. In section 3 we present results of tomographic reconstructions.

The SMILE mission is expected to launch in 2024 into a highly elliptical orbit with an apogee of approximately 19 R_E above the Earth's northern hemisphere. Figure 1 shows the imaging geometry of the mission, including the SMILE orbit, nominal positions and shapes for the magnetopause and bow shock, and the nominal field of view of the Soft X-ray Imager (SXI) camera. The field-of-view of SXI is 27 degrees in the dawn-dusk direction and 16 degrees in the noon-midnight direction, which results in a covered area in the equatorial plane of approximately 9 R_E in the dawn-dusk direction, and 5.5 R_E in the

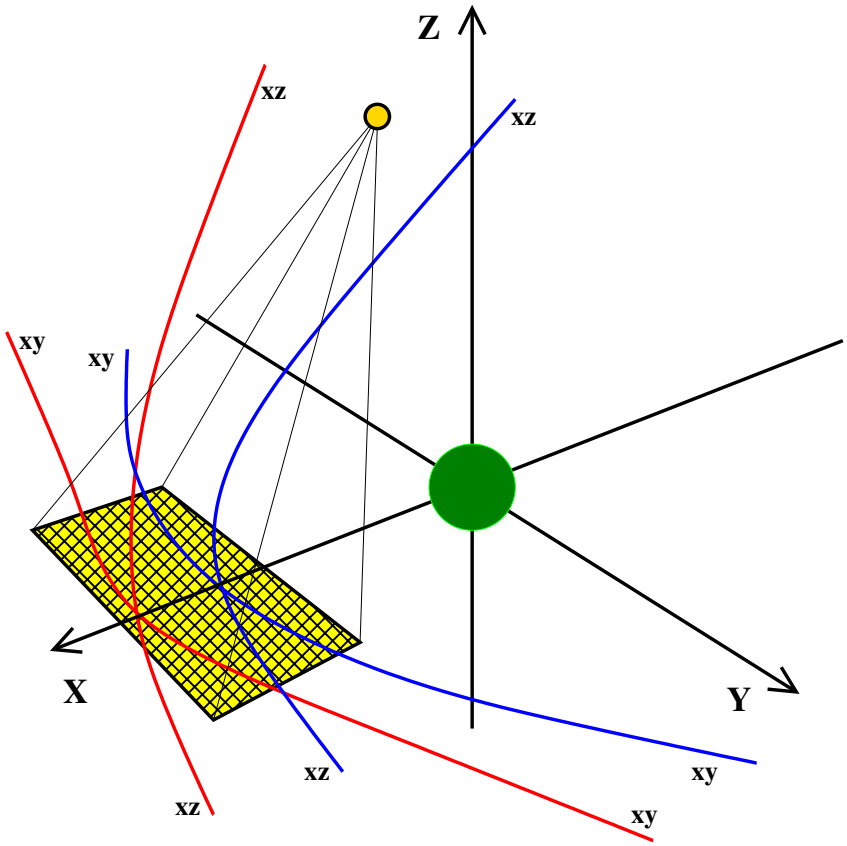

Figure 1. Imaging geometry showing the Earth (in green), the magnetopause (in blue), the bow shock (in red), a nominal imaging position for SMILE of 10-20 R_E North from Earth, and a nominal field-of-view, and its projection onto the XY-plane (hatched, in yellow). The vantage point of this perspective drawing is at +X, +Y, +Z, looking toward Earth.

noon-midnight direction when the spacecraft is at apogee. The SXI CCD detector has 751 pixels in the noon-midnight direction and 1288 pixels in the dawn-dusk direction. The full-width-at-half-maximum (FWHM) of the point-spread function is 8 arcminutes, and the energy range is 0.2 - 5 keV. At the center of the field of view the effective area of the instrument is about 9.6 cm^2 at 0.5 keV. This is approximately flat over about half of the field of view. It then drops (due to vignetting) to about 50% of this at the center of each of the edges of the field of view and about 25% at the corners of the field of view (SXI PI Team, private communication). The dominant spectral line is the soft X-ray emission from the process

$$O^{7+} + H \rightarrow O^{6+} + H^{+} + \gamma \tag{1}$$

In this paper we will follow our earlier paper [*Jorgensen et al.*, 2019a] which used a FWHM of 12 arcminutes which results in images of 75 pixels in the noon-midnight direction and 129 pixels in the dawn-dusk direction. This results in an effective resolution of approximately 0.03 R_E to 0.07 R_E in the equatorial plane for the range of satellite altitude from which SXI is observing.

In addition to this paper exploring reconstruction using a single spacecraft it also sets the stage for exploring reconstruction using multiple spacecraft. There is a possibility that in the near future there will be multiple spacecraft available with imaging capability similar to SMILE/SXI, and in separate papers we will explore that topic.

2 Methodology

We begin by simulating soft X-ray images in the same way as we did in *Jorgensen et al.* [2019a], and which we briefly summarize here in section 2.1. Those images are used as the basis for the tomographic reconstructions, described in section 2.2, with and without total variation minimization regularization (section 2.3), and with or without symmetry (section 2.5).

2.1 Simulating X-ray emissions and images

To simulate realistic X-ray emissions we begin with a simulation from the PPMLR-MHD code, which simulates the solar wind-magnetosphere-ionosphere system. The code was

developed by *Hu et al.* [2007], and uses an extended Lagrangian version of the piecewise parabolic method (PPM) to solve the MHD equation in the spatial region $-300\,R_E \leq x \leq 30\,R_E$, $-150\,R_E \leq y, z \leq 150\,R_E$. The ionosphere is assumed to have a uniform Pedersen conductance and zero Hall conductance, and is coupled to the magnetosphere at $r = 3\,R_E$. Dipole tilt is assumed to be zero in the computations for this paper. The solar wind conditions, number density, speed, and IMF B_z for the simulation are respectively $n_{sw} = 35\,\mathrm{cm}^{-3}$, and $v_{sw} = 400\,\mathrm{km/s}$, and IMF $B_z = -5\,\mathrm{nT}$. From the MHD model the volume emissions rate can be computed by [*Cravens*, 2000]

$$P = \alpha_{cx} n_H n_{sw} \langle g \rangle \quad \left(eV\, cm^{-3}\, s^{-1} \right) \tag{2}$$

where α_{cx} is the efficiency factor integrated over all species and transitions, defined as

$$\alpha_{cx} = \sum_s f_s \sum_q f_{sq} \sigma_{sq} \sum_j f_{sqj} \Delta E_{sqj} \tag{3}$$

The sums are over solar wind heavy ion species s, charge state q, and the transition index j. f_s is the fraction of the solar wind ions which is species s, f_{sq} is the fraction of those which is in charge state q, and f_{sqj} is the probability of transition from charge state q to $(q-1)$ by charge-exchange. ΔE_{sqj} is the transition energy σ_{sq} is the charge transfer cross section. More details about α_{cx} are provided by *Cravens* [1997] and *Sun et al.* [2015]. *Cravens* [2000] estimated that α_{cx} ranges between 6×10^{-16} and 6×10^{-15} $\mathrm{eV/cm^2}$. As in our earlier paper we thus adopt $\alpha_{cx} = 1.0 \times 10^{-15}$ $\mathrm{eV/cm^2}$. Returning to equation 2, n_H is the density of the Earth's exosphere, n_{sw} is the number density of the solar wind, and $\langle g \rangle = \sqrt{u_{sw}^2 + u_{th}^2}$ is the average collision speed which is the geometric average of the solar wind bulk speed, u_{sw}, and thermal speed, u_{th}.

The resulting X-ray emissions are shown in Figure 2, with a GSM XY slice in panel a and a GSM XZ slice in panel b. The X-ray emissions from inside the magnetopause are negligible and thus set to zero (refer to *Sun et al.* [2019] for more details of the MHD simulation data and how they are processed to produce the data set we use here). The cusp emission close to the inner boundary ($r < 5\,\mathrm{R}_E$) is not considered in the current study to avoid the boundary effect. At the inner boundary the number density is high, essentially plasmasphere densities, but the density of highly-charged heavy ions is much lower. Thus the procedure used to simulate X-ray emissions will not produce a realistic

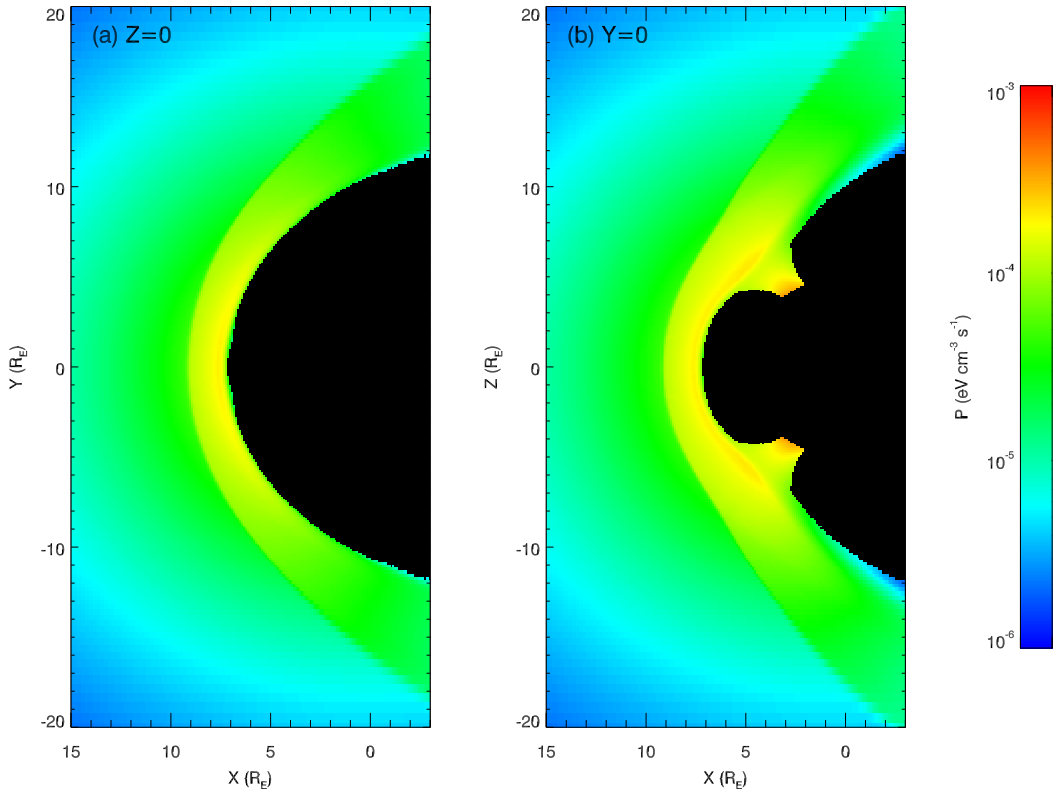

125 **Figure 2.** X-ray emissions based on the MHD model. (a) XY plane cross-section, (b) XZ plane cross-

126 section.

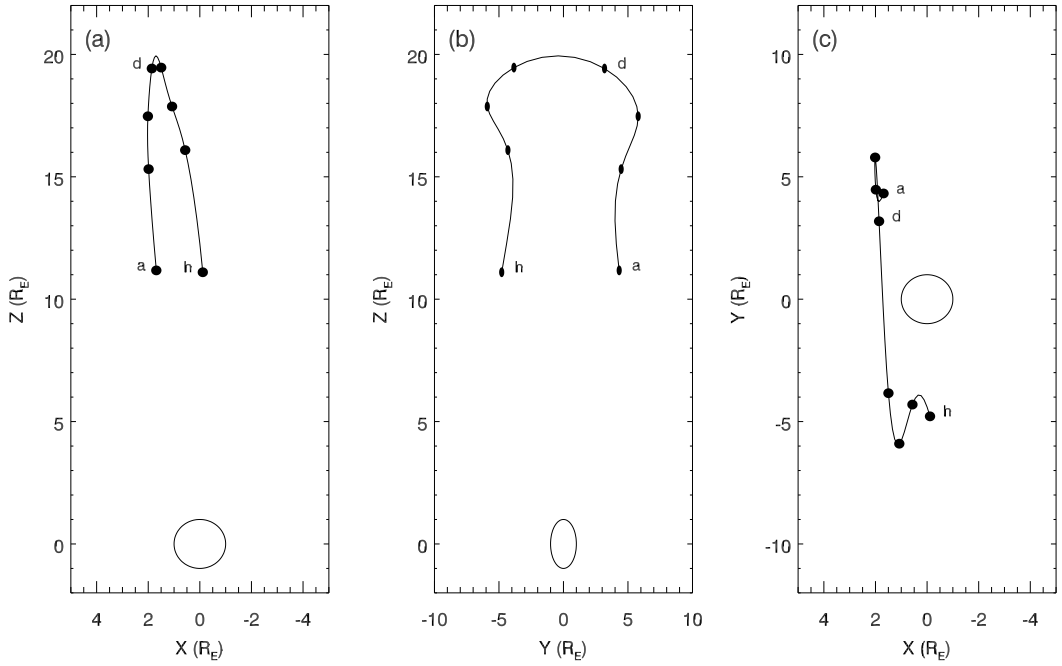

Figure 3. SMILE spacecraft positions, in GSM coordinates, for a portion of a simulated orbit, for the simulation interval 2021/9/30 23:00:00 to 2021/10/2 12:00:00, corresponding to points which have $R \geq 12\,R_E$. Panel (a) is the XZ plane, (b) the YZ plane, and (c) the XY plane. The dots and associated labels refer to images in Figure 4, and the circle in each plot is the Earth.

flux in this region. It is also not necessary to model this region because it is only rarely imaged by SMILE SXI [*Sun et al.*, 2021]. From the X-ray volume emissions X-ray images can be computed. The emissions are optically thin such that the intensity along a line of sight is given by

$$I = \frac{1}{4\pi} \int P\,dl \quad \left(eV\,cm^{-2}\,s^{-1}\,sr^{-1}\right) \tag{4}$$

which can be converted into an irradiance image by multiplication by the geometric factor G $\left(cm^2\,sr^1\right)$ for each pixel, and converted into a counts expectation image by dividing by the energy, E, per photon, and multiplying by the integration time, Δt. Figure 3 shows part of one apogee pass of an orbit from one early SMILE orbit simulation, not long after launch, in GSM coordinates. Figure 4 shows examples of intensity images for that apogee pass. The magnetopause is clearly visible, and in many of the images both cusps are visible as well.

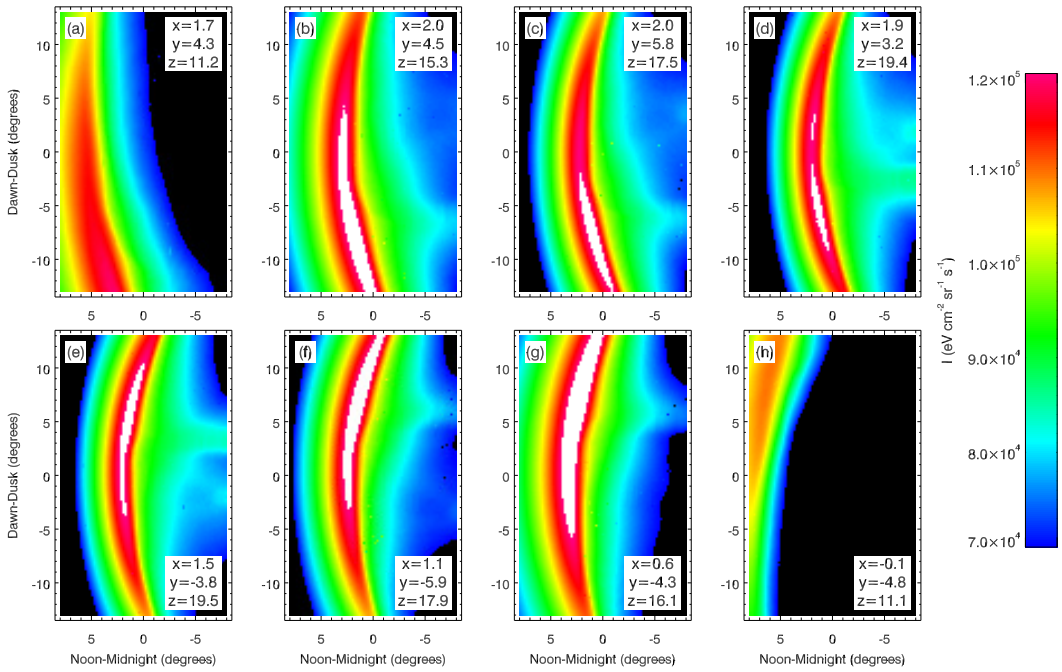

Figure 4. Simulated intensity images of the X-ray emissions in Figure 2 using Equation 4 for the apogee pass in Figure 3.

2.2 Tomographic reconstruction method

The reconstruction method we will use resembles that used in medical imaging. An optically thin object (often referred to as a "phantom") emits radiation isotropically (our phantom is in Figure 2). A sensor collects images of the phantom from a diverse range of viewing angles, the images in Figure 4.

In a discretized world the imaging process which we described above can also be expressed in a single matrix equation,

$$\bar{\bar{A}}\,\bar{u} = \bar{p} \tag{5}$$

where $\bar{u}$, of length n, represents the three-dimensional emission, $\bar{p}$, of length m, represents all of the pixels in all of the images, and $\bar{\bar{A}}$ is a geometry matrix, with m rows and n columns. In $\bar{\bar{A}}$ each element a_{ij} then represents how much volume element j contributes to pixel i. Equally, it can be described as being the length of the ray of pixel i which is inside volume element j. Tomographic reconstruction then solves the inverse problem of determining $\bar{u}$ from $\bar{p}$ given a known geometry matrix $\bar{\bar{A}}$. In the most general case the

problem does not have a single unique solution so various constraints must be employed, and accurate tomographic reconstruction, especially for medical applications, is an active area of research. For this work we use one of the earliest and simplest reconstruction techniques, the Algebraic Reconstruction Technique (ART) [*Gordon et al.*, 1970]. ART is an iterative relaxation reconstruction approach. In our implementation, at each iteration, k, we cycle through the rays, $i \in [1; m]$ and compute the next emissions distribution, $\bar{u}^{k+1}$ as

$$\bar{u}^{k+1} = \bar{u}^{k} + \lambda_k \frac{p_i - \bar{A}_i \cdot \bar{u}^{k}}{||\bar{A}_i||^2} \bar{A}_i^T \tag{6}$$

Where λ_k is a relaxation parameter for each iteration, and $\bar{A}_i$ is row i of $\bar{\bar{A}}$. One iteration, e.g. k to $k+1$ consists of m computations of equation 6, one for each pixel in the images or row in the geometry matrix $\bar{\bar{A}}$. Even with this procedure there is still some choices to be made, e.g. the values of λ_k, as well as some detailed choices of precisely how Equation 6 is implemented. E.g. the order in which the pixels are visited and used in Equation 6, and whether $\bar{u}^k$ on the right-hand side of the equation is updated between pixels or only after all pixels are visited. We made the choice of randomizing the order in which the pixels are visited and preserving that random order for all iterations, k, and the choice to update $\bar{u}^k$ as each pixel is visited. The iterations in Equation 6 continue until either 100 iterations have been completed or until the total absolute change over the reconstruction volume in one iteration is less than 0.1% of the total absolute value. In cases where 100 iterations are completed the change per step is still small, typically 0.3% or less.

The matrix $\bar{\bar{A}}$, if fully evaluated, will be extremely large. However, it is not necessary to evaluate all elements of $\bar{\bar{A}}$, because in an approximately cubic reconstruction volume such as we are using here, the vast majority of the elements in $\bar{\bar{A}}$ have zero value. This is because a given ray, corresponding to a given pixel, only pass through a small fraction of the cells in the volume. For a reconstruction volume of dimension N on each of 3 sides, the number of cells touched by a ray will be of the order N (multiplied by a constant of the order 1). Thus while each row of $\bar{\bar{A}}$ has N^3 elements, only of the order of N of those are non-zero. In other words, only the fraction $1/N^2$ of the elements of $\bar{\bar{A}}$ are non-zero.

Let's consider a numerical example: We begin with a 100 by 100 by 100 reconstruction volume, or 10^6 cells. Next let's assume 10 images of that volume, each of dimension 100 by 100. That totals 10^5 pixels. The dimensions of $\bar{\bar{A}}$ are then $m = 10^5$ rows by

$n = 10^6$ columns or 10^{11} elements, an extremely large matrix. However, the number of non-zero elements in each row is of the order of the linear dimension of the reconstruction space. So in each row of the order of 100 elements, perhaps up to a few hundred out of 10^6 will be non-zero. That means that in this case, approximately 99.99% of the elements will be zeros. By storing only the non-zero elements of $\bar{\bar{A}}$ a tremendous amount of storage can be saved. Furthermore, because multiplication by zero takes as much computation as multiplication by any other number a tremendous amount of computation can be saved by not carrying out those unnecessary operations. Practically we implement this sparse matrix by creating a list, for each pixel, of the volume elements that the ray intersects, and the length of that intersection.

2.3 Total variation minimization regularization

In the above example there are 10^6 cell values to be determined based on 10^5 pixel values. The problem is not well-constrained. For many practical cases the ART procedure is nonetheless capable of producing an adequate reconstruction of the original volume distribution. However, for more complex volume distributions, when there is noise present in the images used for the reconstruction, or to improve the accuracy of the reconstruction, additional constraints can be introduced. This is known as regularization of the inversion problem. One of these regularization approaches, the one which we use in this paper, is an image denoising technique called total variation (TV) minimization which works by reducing the total pixel-to-pixel variation in the image, subject to some constraints, [*Rudin et al.*, 1992].

Chambolle [2004] defines the total variation in the case of a 2D image and we extend it to a 3D volume, v, as follows

$$J(v) = \sum_{i,j,k} \left| \bar{\nabla}(v)_{ijk} \right| \tag{7}$$

Where $1 \le i \le N_X$, $1 \le j \le N_Y$, and $1 \le k \le N_Z$, $\vec{\nabla}$ is the gradient, and $|\cdot|$ signifies the geometric norm (square root of sum of squares of coordinates). The purpose of total variation minimization is then to determine a volume, u, which is similar to the volume v, but has smaller total variation. The extent to which u and v are similar is from the total mean-squared difference between them

$$E(u,v) = \sum_{1\le i\le N_x, 1\le j\le N_y, 1\le k\le N_x} \left(v_{ijk} - u_{ijk}\right)^2 \tag{8}$$

Minimizing the total variation while keeping u similar to v can then be formulated as this weighted minimization problem,

$$\min\left[E(u,v) - \lambda J(u)\right] \tag{9}$$

where λ is a parameter, the regularization parameter, or the denoising parameter, which determines the relative importance of minimizing the total variation versus making u similar to v. If $\lambda = 0$ then $u = v$, while as $\lambda \to \infty$, u becomes a constant.

From the above equation it is not immediately obvious how to determine u. A number of approaches have been developed over the years, and new efficient minimizers continue to be developed. We use the method presented by *Chambolle* [2004] and $\lambda = 10^{-3}$.

2.4 Combining ART and Total Variation Regularization

We combine ART and TV regularization by running one or more iterations of the TV algorithm after one or more iterations of the ART algorithm. One ART iteration consists of evaluating equation 6 successively for every pixel of every image in the random order established at the start of the reconstruction.

2.5 Symmetry

Under certain conditions the magnetosphere can be viewed as being approximately symmetric around a plane or an axis. Symmetry cannot be assumed for all situations, but the relatively small field of view of SMILE means that it is observing only a small portion of the sub-solar magnetopause and bow-shock, which means that there are circumstances where that portion will have a simple symmetric shape. The symmetry plane or axis must be chosen according to the actual geometry. In the case of the model in Figure 2 North-South symmetry is an excellent assumption. We will show how assuming symmetry can improve the reconstruction results. We incorporate symmetry by including a second set of images which are recorded from a point symmetrically opposite through the X-axis, in the opposite hemisphere from the simulated SMILE location, and looking at the same tar-

$Z(R_E)$	R_{mhd}	R_3	R_{10}	R_{30}	R_{100}	R_{200}	σ_3	σ_{10}	σ_{30}	σ_{100}	σ_{200}
0	7.7	8.9	7.9	7.9	8.3	8.1	0.69	0.3	0.32	0.3	0.29
4	6.4	6.4	6.4	6.4	6.3	6.3	0.49	0.24	0.33	0.27	0.34
5	5.5	6.3	6.1	6.1	5.7	5.6	0.49	0.27	0.33	0.23	0.20

Table 1. Measurements from the reconstructions in Figure 5. Each row represents one of the three cuts shown in panel a, first row for $Z = 0$ (blue), second row for $Z = 4$ (green), and third row for $Z = 5$ (red). The Radii, $R.$ are where the emission is maximum, with R_{mhd} for the MHD model Figure 2, and R_i ($i = 3, 10, 30, 100, 200$) are measured on the reconstructions in panels a, b, c, d, e. The values of σ_i are RMS differences between MHD model and reconstruction, as described in the text.

get point. This means that we can use the same reconstruction algorithm and not have to create a reconstruction algorithm which imposes symmetry directly.

3 Results

Next we evaluate the ability of the tomographic reconstruction algorithms outlined above to reconstruct the X-ray emission distribution from the SMILE mission. We show three different reconstructions. Firstly, we show single-orbit reconstruction illustrating the difference between ART alone, ART with TV regularization, and ART with TV regularization and symmetry, showing the difference between using different numbers of images, different numbers of TV iterations, and symmetry or not. Secondly, we show a noise-free reconstruction using observations spread over a year, with approximately 100 images, using TV regularization and symmetry. Thirdly, we show the same reconstruction with images spread over a year, but using noisy images with low SNR for the reconstruction, and TV regularization.

3.1 Noise-free reconstructions

We begin by reconstructing the emissions from a single orbit. The SMILE SXI only produces useful data when the spacecraft is in the magnetosheath or solar wind. We model that behavior by only recording images when the spacecraft GSM Z-coordinate is greater than $10\,\mathrm{R}_E$. Figure 3 shows the orbit plot. Notice that the spacecraft GSM X-coordinate only varies over a range of $3\,\mathrm{R}_E$ during the orbit whereas the GSM Y-coordinate varies by

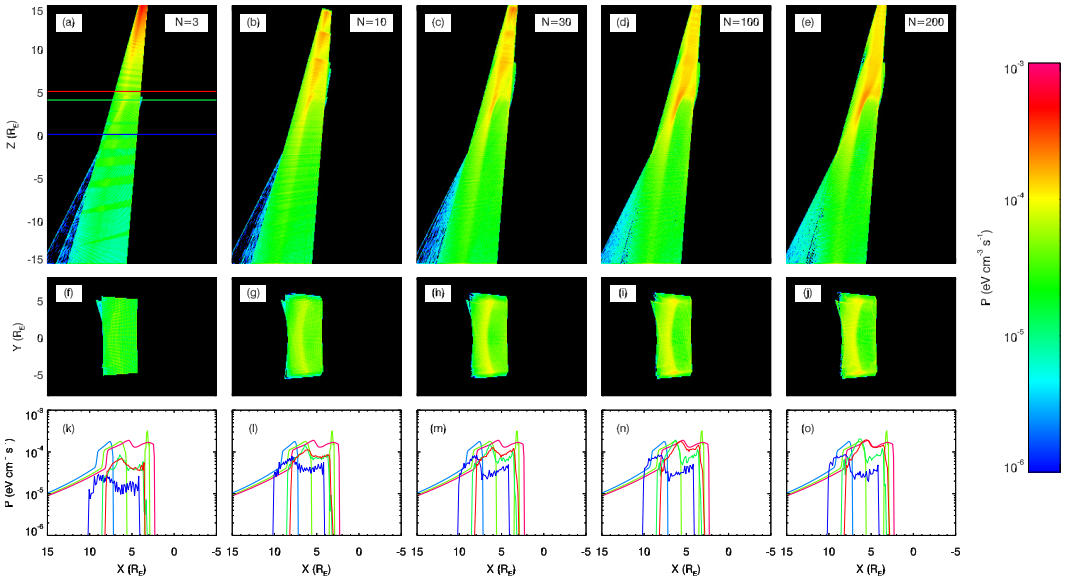

Figure 5. Reconstruction using ART with different numbers of images (3, 10, 30, 100, 200 from left to right) spread evenly over the orbit segment in Figure 3. The top row, panels a to e, are cuts along the XZ (meridional) plane at $Y = 0$. The center row, panels f to j, are cuts along the XY (equatorial) plane at $Z = 0$. The first column, panels a and f, is a reconstruction using three images, the second column, panels b and g, ten images, the third column, panels c and h, 30 images, the fourth column, panels d and i, 100 images, and the fifth column, panels e and j, 200 images. In the bottom row are linear cuts through the reconstructions (thin curves) parallel to the X-axis at $Y = 0$ and $Z = 0$ (blue), $Z = 4$ (green), and $Z = 5$ (red). The thick curves are the corresponding cuts through the MHD model Figure 2.

more than $10\,R_E$. Figure 5 shows the reconstruction using the simple ART algorithm. The first column uses 3 images, separated by approximately 10 hours, the second column 10 images separated by approximately 3.3 hours, the third column 30 images separated by approximately 1 hour, the fourth column 100 images separated by approximately 20 min, and the fifth column 200 images separated by approximately 10 minutes. The top row shows a meridional cut (The XZ-plane, $Y = 0$), the second row an equatorial cut (The XY-plane, $Z = 0$), and the third row plots of emission along the lines of corresponding color in panel a. In the panels in the top row it appears that the northern portion of the magnetosheath is reconstructed somewhat, and that a portion of the cusp is reconstructed as well, except in panel a, possibly panel b. In Table 1 are several measures of performance. The first row is for the $Z = 0$ (blue) cut, the second row is for $Z = 4$ (green) cut, the third row is for $Z = 5$ (red). The first column is the location of peak emission in the MHD model, the following five are the locations of peak emission in the reconstruction, and the last five are RMS differences between the MHD model and the reconstruction. Those measures are computed as the

$$\sigma^2 = \frac{1}{N}\sum_{i=1}^{N}\left(\log_{10} P_{\mathrm{MHD}} - \log_{10} P_{\mathrm{R}}\right)^2$$

where N is the number of points sampled, P_{MHD} is the emission in the MHD model and P_R is the emission in the reconstruction. The sum is over those points for which both the MHD model and the reconstruction have values greater than 10^{-5}. In other words, use only points where the MHD model had non-zero flux, and only the points in the reconstruction which were imaged. What we see is that the reconstruction is better at $Z = 4$ and $Z = 5$, and worse in the equatorial plane. These regions are closer to the imager and that may be the reason for the better reconstruction. We also see that increasing the number of images used in the reconstruction improves the reconstruction, possibly plateauing between 30 and 100 images. From that we conclude that 100 images is sufficient, and we use 100 images in the rest of the papers. As more images are added the location of the peak emission also approaches that in the MHD model, but better in the two positive-Z traces. The values $R_{100} = 8.3$ for the $Z = 0$ trace is due to noise. Upon close examination we see that there is also a peak close to $X = 8.0$, but is is slightly lower in amplitude. Overall the reconstructions produce smaller values of P than the MHD model. We believe this is a result of the small range of viewing angles, giving insufficient constraints, resulting in a less

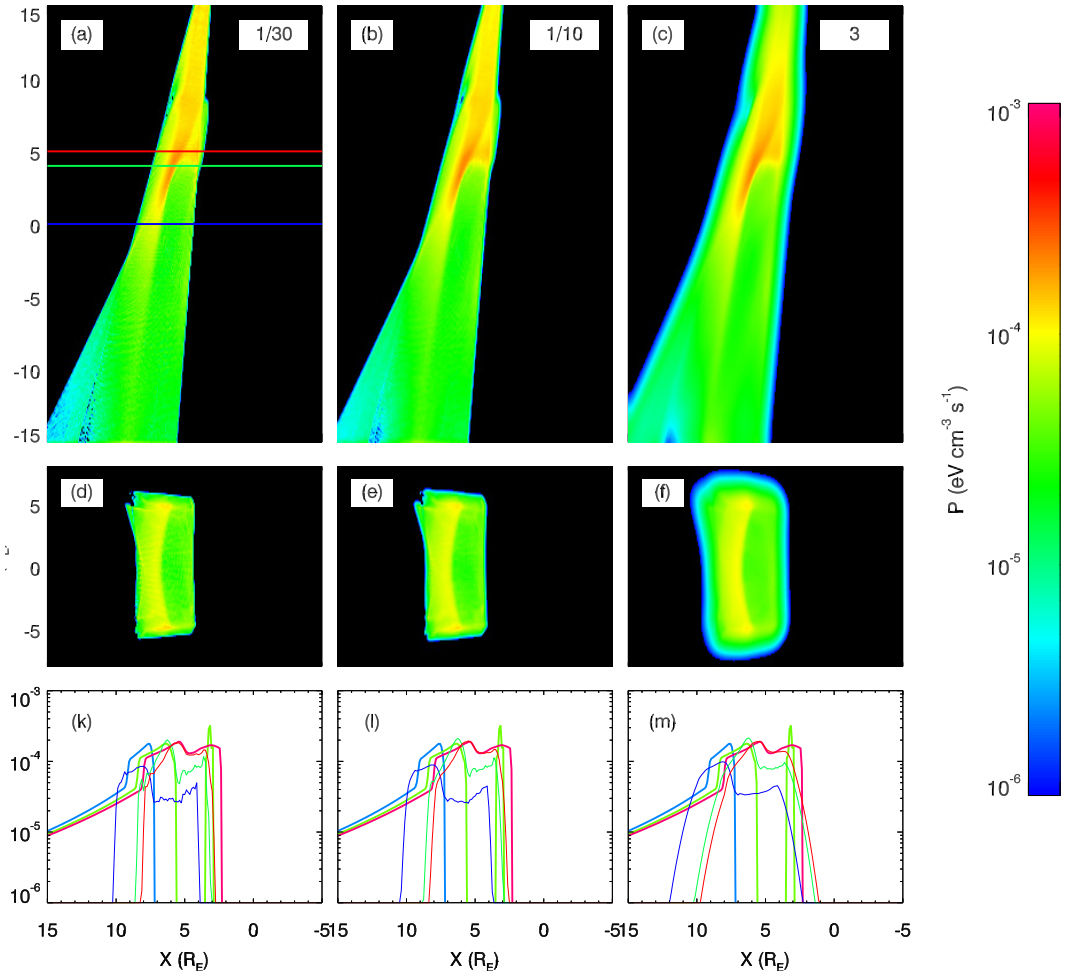

Figure 6. Reconstruction using 100 images and three different numbers of TV iterations. The figure elements are the same as in Figure 5. The first column is for one TV iteration every 30 ART iterations, second column is for one TV iteration every 10 ART iterations, and third column for 3 TV iterations every ART iteration.

than optimal reconstruction. When an ART reconstruction is not sufficiently constrained it will tend to distribute the emission along the ray paths, and that is what we see in the top row of the figure.

Figure 6 shows the reconstruction including TV regularization. As in Figure 5 the top row is for the XZ ($Y = 0$) slice, and the bottom row is for the XY ($Z = 0$) slice. 100 images are used in all reconstructions. The first column, panels a and d, is for one TV iteration every 30 ART iterations, the second column, panels b and e, for one TV iterations every 10 ART iterations, the third column, panels c and f, is for 3 TV iterations

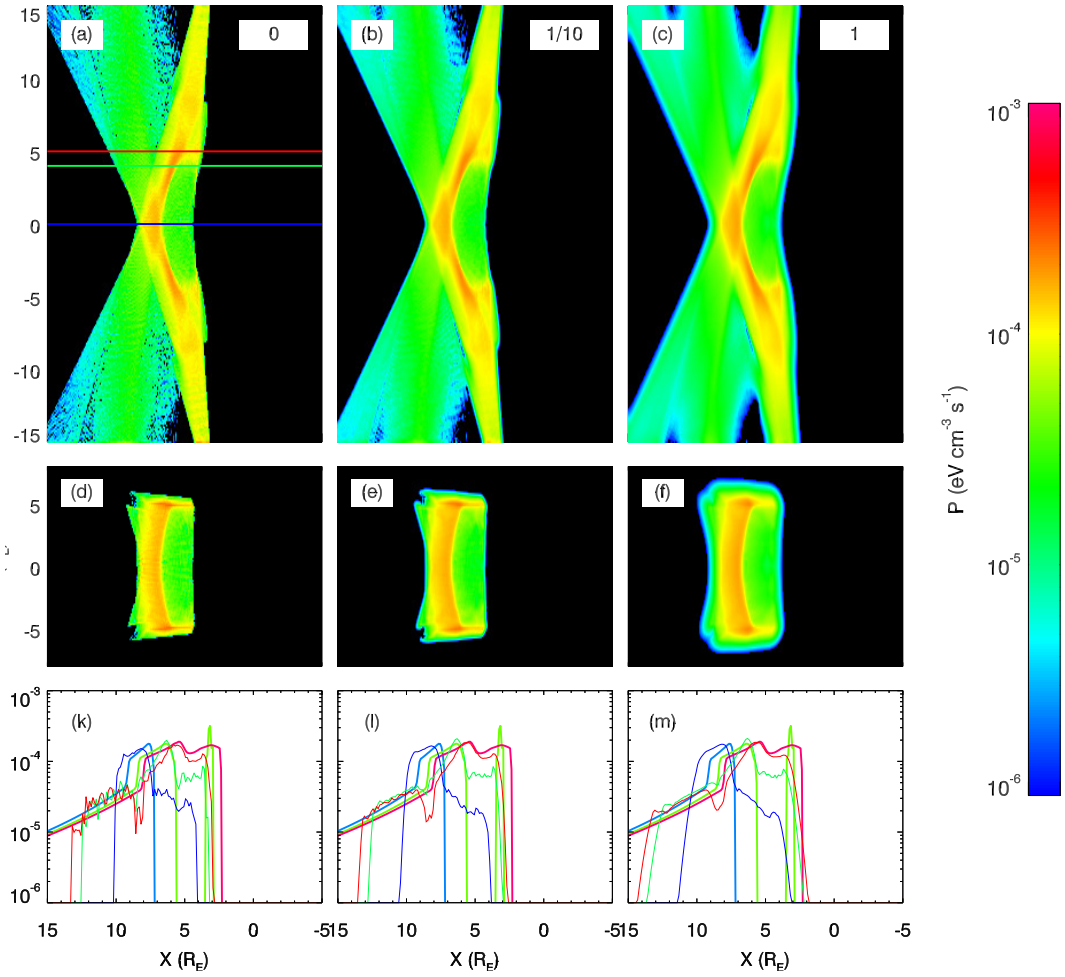

Figure 7. Reconstruction with symmetry. The layout of this figure is similar to Figure 5. The first column, panels a, d, k is without TV, the second column is for one TV iteration every 10 ART iterations, and the third column is for one TV iteration every ART iteration.

every ART iterations. As expected, the resulting reconstructions show less pixel-to-pixel variation (some is still visible in the $Z = 0$ (blue) and $Z = 4$ (green) traces in panels k and l), because that is what the TV regularization is intended to do. Aside from this TV has little effect on the reconstruction, except that for three TV iterations there is some noticeable smoothing. This suggests that for noise-free reconstructions one TV iteration every few ART iterations is sufficient for smoothing.

Figure 7 is the reconstruction when symmetry is invoked. We assume that the reconstruction is symmetric about $Z = 0$. We can think of two fundamental ways of imposing symmetry on the problem. One is to modify the algorithm to impose symmetry. Another

$Z(R_E)$	$R_{\mathrm{mhd}}(R_E)$	$R_0(R_E)$	$R_{1/10}(R_E)$	$R_1(R_E)$	σ_0	$\sigma_{1/10}$	σ_1
0	7.7	8.2	8.2	8.2	0.26	0.27	0.28
4	6.4	6.3	6.3	6.3	0.23	0.19	0.21
5	5.5	5.8	5.6	5.7	0.21	0.20	0.24

Table 2. Measurements from the reconstructions in Figure 7. These are computed in the same way as the measurements in Table 1. The three columns R_0 to R_1 are the radii of peak reconstructed emission based on the three corresponding columns in Figure 7, and the three columns σ_0 to σ_1 are the RMS differences as described in the text.

is to double the number of images with the second half being duplicates of the original images, appropriately mirrored, and with a vantage point which is the appropriate mirror point of the original images. We chose the latter way of doing it as the exact same algorithm can be used for both problems, at the expense of some additional computation. The second set of images have vantage points which are the mirror point around the X-axis (so same X-coordinate, negative of the Y- and Z-coordinates). This will not result in exact symmetric reconstruction because of the random order in which the pixels are visited, but the asymmetry is much smaller than any other artifacts in the reconstruction. We find that this small algorithmic difference is unimportant in gauging the effect of imposing symmetry. in Figure 7 the first column is without TV regularization, the second is for one TV iteration every 10 ART iterations, and the third is for one TV iteration every ART iteration.

Both the northern and southern magnetosheath are reconstructed, as expected, but there are a several artifacts in the images. The magnetosheath is not curved in the same way as the original X-ray emissions in Figure 2. Instead the northern and southern portion each have a more linear shape, that shape being aligned closely with the direction to apogee ($X = 1.5\,\mathrm{R}_E$, $Z = 20\,\mathrm{R}_E$, see Figure 1). This is precisely the result one expects from the ART algorithm when the rays point mostly in the same direction; in the absence of other information, the brightness will be distributed along the ray. This suggests that while using symmetry does improve the reconstruction near the equator, the range of ray look-directions is the limiting factor in the accuracy of the reconstruction. Table 2 shows the same type of statistics as in Table 1. Overall the quality of the reconstruction is sim-

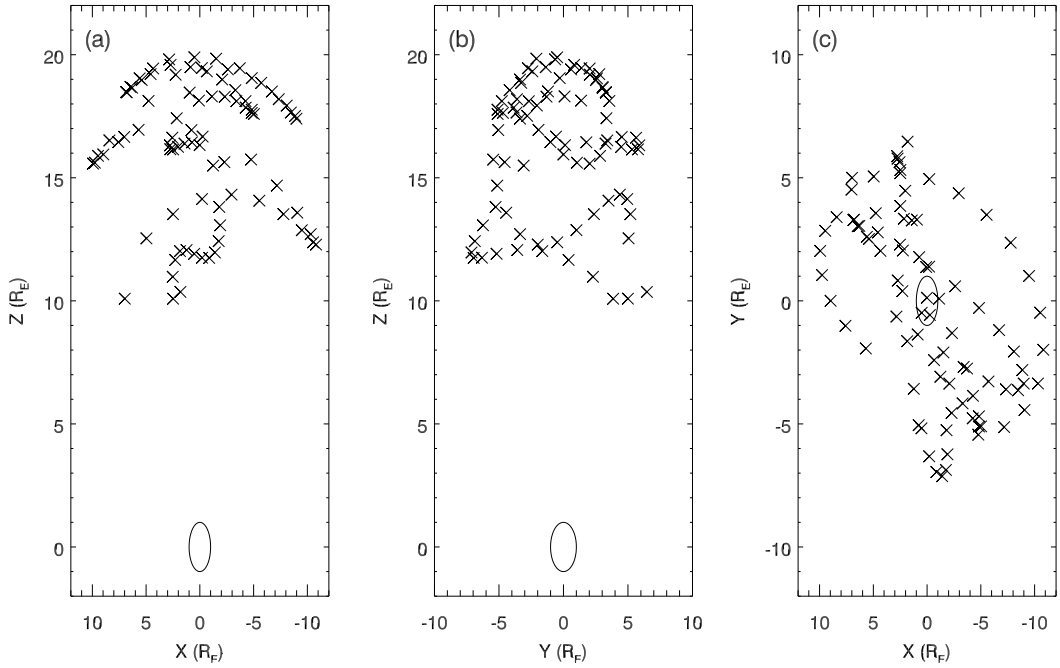

Figure 8. Location of SMILE at similar UT (4, 5, or 6 UT), approximately evenly spread through one year. (a) XZ plane, (b) YZ plane, (c) XY plane.

ilar to the previous exampls. In the next section we will expand the range of ray look-directions.

3.2 Superposed epoch

The single-orbit reconstruction assumes that the magnetosheath looks unchanged for the 30+ hours of the apogee section of the orbit. That requires constant solar wind conditions which is rare for that length of time, but it also ignores the change in the dipole tilt. It is likely possible to correct for the dipole orientation however; since the portion of the sub-solar portion of the magnetosheath imaged is small it is likely sufficient to adjust the location and look direction of the camera to compensate for the dipole tilt. We plan to investigate this in the future.

Another approach is a true superposed-epoch reconstruction using images widely spaced in time, for similar UT (to have the same dipole orientation), and for similar solar wind conditions. In this section we simulate that scenario. We only address the question of whether the resulting superposed epoch geometry is sufficient for the reconstruction, not whether it is actually possible to find a sufficiently large number of images over an ex-

tended period of time with sufficiently similar conditions. The question of what constitutes the necessary criteria for "sufficiently similar conditions" can be addressed in simulation or with future observational data. A bootstrap analysis will reveal whether the selected images produce a consistent reconstruction with small uncertainty. This is done by selecting multiple random samples (of size N) from a collection of N candidate images, doing the reconstruction and then doing a statistical analysis over the ensemble of reconstructions. We do intend to address this in the future, but it is a significantly larger computational task than all the other computations in this paper and beyond the scope of this paper.

For the geometrical analysis we simulate images over a period of a year which have nearly the same UT. In Figure 8 we show the locations of SMILE approximately every 72 hours for one year, when the GSM Z-coordinate is greater than $10\,R_E$. The points in Figure 8 were derived as follows. For one year step through the orbit file by 72 hours, recording an image at 4, 5, and 6 UT, if the satellite position Z-coordinate is at least $10\,R_E$. Then use every third of such images, for a total of 87 images. We have concluded from the previous simulations that 100 images are likely sufficient.

Comparing Figure 8 to Figure 3 it appears that the former contains a larger range of satellite positions, which means a larger range of look directions through the reconstruction volume, which will likely result in a better reconstruction.

Figure 9 shows the reconstruction for noise-free images using both TV regularization and symmetry. The reconstruction is, visually, much better than that in Figure 7. Figure 9 has the same arrangement of panels as Figure 7 so the two can be compared directly. Table 3 are the same measurements as in earlier tables, and there we can see a significant improvement. All emission peaks are within one resolution element of each other, and the RMS difference between the MHD model and the the top row is smaller as well. The magnetosheath in this reconstruction looks much more like that in Figure 2, with a similar curvature (as opposed to the angular look in Figure 7), and fewer reconstruction artifacts. One notable artifact is a ghost emission peak near the equatorial plane sunward of the magnetosheath. From this simulation it appears that good reconstructions can be made from a single orbit using superposed epoch combination of images over a period of a year, a complete rotation of the Earth under the orbit.

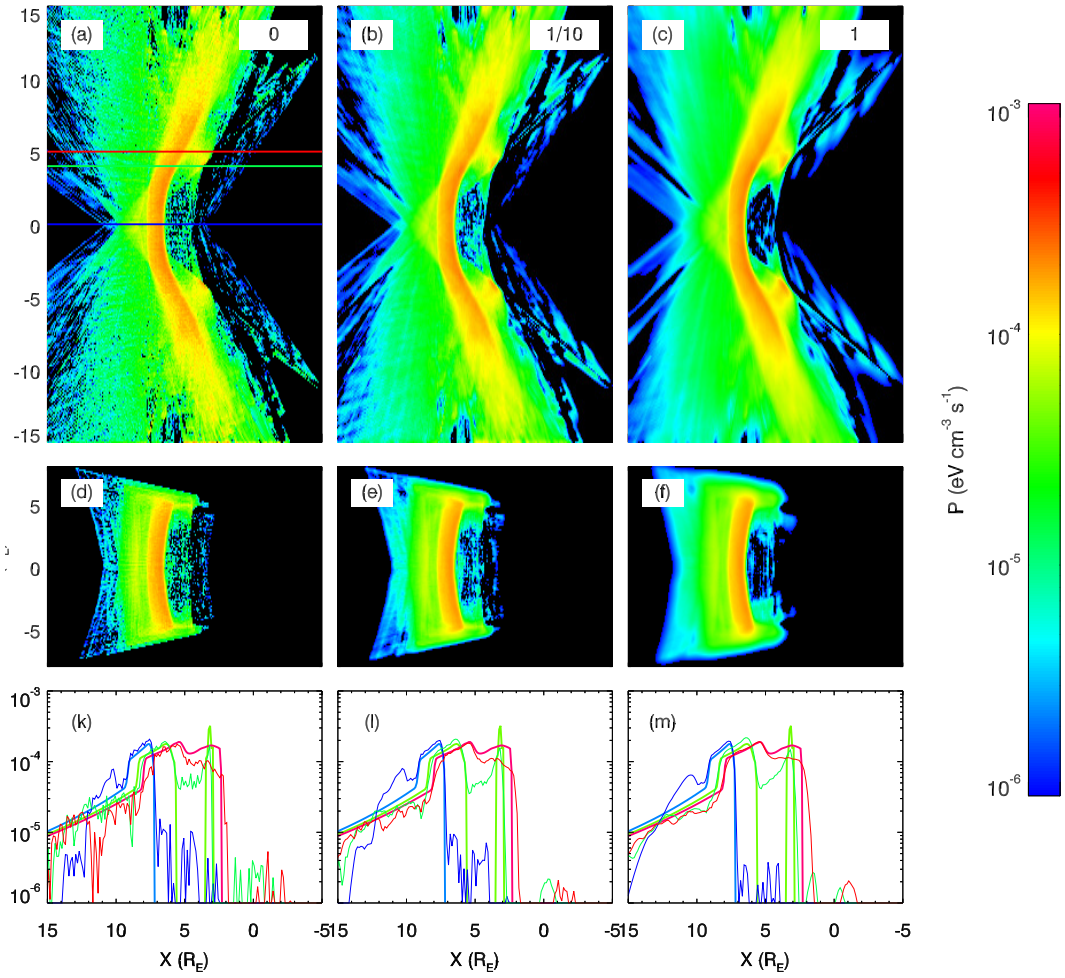

406 **Figure 9.** Reconstruction using 87 noise-free images recorded at the points marked in Figure 8. The re-
407 constructions use TV regularization, and symmetry. The layout of the figure is the same as Figure 7, and the
408 three columns are for the same number of TV iterations as in Figure 7, no TV for the first column, one TV
409 iteration every 10 ART iterations for the second column, and one TV iteration every ART iteration for the
410 third column.

$Z(R_E)$	$R_{\mathrm{mhd}}(R_E)$	$R_0(R_E)$	$R_{1/10}(R_E)$	$R_1(R_E)$	σ_0	$\sigma_{1/10}$	σ_1
0	7.7	7.6	7.6	7.7	0.16	0.19	0.17
4	6.4	6.4	6.4	6.4	0.12	0.11	0.10
5	5.5	5.6	5.6	5.4	0.17	0.12	0.09

411 **Table 3.** Measurements from the reconstructions in Figure 9. The layout of this table is identical to Table 2.

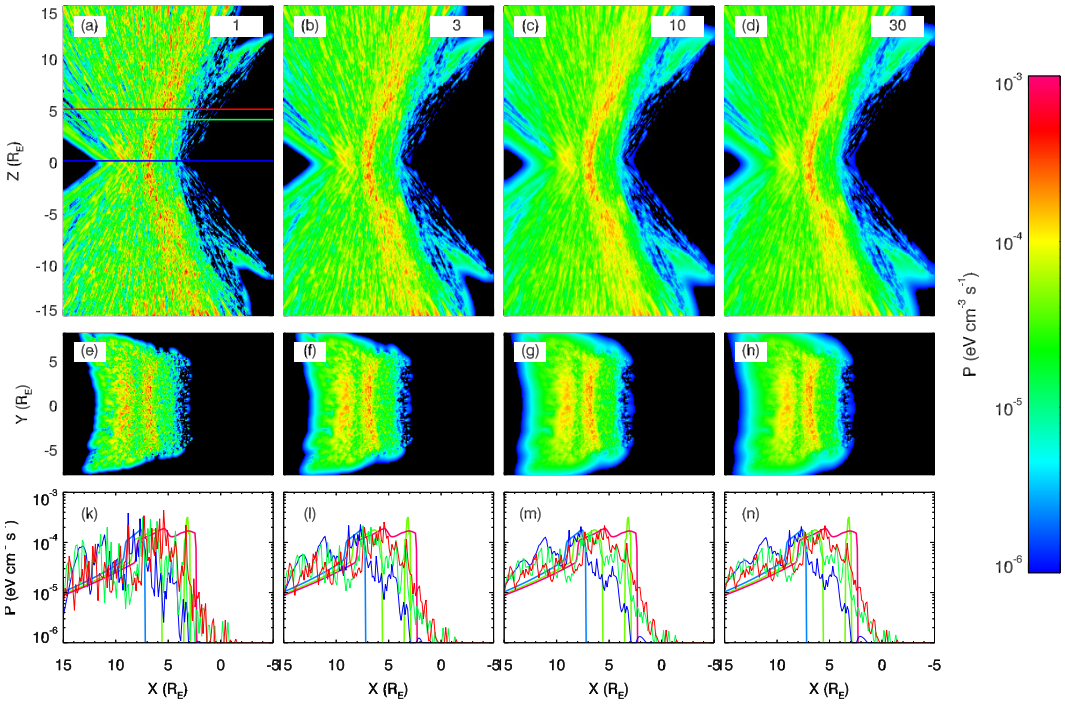

Figure 10. Meridional cuts (XZ plane for $Y = 0$) through reconstructions with noisy images each with 1 count per pixel, with different number of TV iterations; (a) 1, (b) 3, (c) 10, (d) 30.

3.3 The effect of Poisson noise

In the previous we have reconstructed using noiseless images, which is not realistic in most situation. To explore the effect of Poisson noise on the reconstruction we repeat the reconstructions from the previous section (which resulted in Figure 9) but using images which contain Poisson noise. We do the reconstruction for images with integration times which result in an average of one count per pixel, and using varying amounts of TV regularization. The reconstruction results are shown in Figure 10, with the first column showing one TV iteration per ART iteration, the second column showing 3 TV iterations per ART iteration, the third column showing 10 TV iterations per ART iteration, and the fourth column showing 30 TV iterations per ART iteration.

In Figure 10 we see that TV regularization has a significant effect on the accuracy of the reconstruction. The magnetosheath is reconstructed better with larger numbers of TV iterations, but there are also problems. A false peak appears in the equatorial region sunward of the magnetosheath. Additionally, the cusp region is not reproduced as well. Nevertheless, it is possible to reconstruct to an extent even with images which have noise

$Z(R_E)$	$R_{\mathrm{mhd}}(R_E)$	$R_1(R_E)$	$R_3(R_E)$	$R_{10}(R_E)$	$R_{30}(R_E)$	σ_1	σ_3	σ_{10}	σ_{30}
0	7.7	8.8	7.7	7.7	7.7	0.44	0.36	0.35	0.35
4	6.4	7.4	7.4	6.7	6.7	0.46	0.39	0.37	0.36
5	5.5	5.4	5.4	5.4	5.4	0.47	0.36	0.36	0.36

Table 4. Measurements for Figure 10. This table is organized as Table 3.

near 100% of the average counts. Table 4 shows the same kinds of measurements as the previous tables. For smaller number of TV iterations the measurements of the locations of peak intensity are dominated by noise. But for larger numbers of TV iterations the peaks are close, within about $0.2\,R_E$, of the peak location in the MHD model. The standard deviations are dominated by noise and not a particularly useful statistic in this case.

4 Discussion

In this paper we have demonstrated that it is possible to tomographically reconstruct large-scale structures in the magnetosphere using multiple images from a single spacecraft. In this case we demonstrated it for X-ray emissions from the magnetosheath, but many of the principles apply more generally. However it should be said that the accuracy of the reconstruction is greatly affected by the range of viewing angles available for the reconstruction. We found that a reconstruction using images distributed over an entire year, with orbit precession in the Earth-Sun coordinate system gives rise to a larger range of viewing angle and substantially improves the reconstruction.

Using regularization, in this case an image-processing algorithm called total variation minimization, improves the reconstruction, as does the assumption of symmetry which was possible in this particular case. There are other possible regularization constraints that can be applied to this reconstruction problem, including physics-based constraints, which should be explored further in the future.

Spurious responses is a well-known feature of tomographic reconstructions, and much effort is made to minimize its effect in the medical field where a bad reconstruction could lead to an incorrect diagnosis. In the future we will consider whether there are techniques from the medical literature which can be used here. However it should be noted that there are some significant differences between medical imaging and the kind of

imaging we are doing. Often in medical imaging there is a very large range of viewing angles, better signal-to-noise ratio, and better control of the geometry of the problem. On the other hand a patient's life does not depend on the accuracy of our reconstructions.

The large improvement of the reconstruction with a relatively modest increase in the range of viewing angles naturally leads one to ask how well the reconstruction would work with a multi-spacecraft mission which provides multiple simultaneous vantage points, and potentially instantaneous reconstructions. In-fact there is the possibility that there will be multiple spacecraft with soft X-ray imaging instruments similar to SMILE SXI in the near future. We are working on preparing a separate paper which explores this topic.

5 Conclusion

This paper is an initial exploration of using SMILE data with tomographic reconstruction techniques. We explored four different areas; the reconstruction using observations from a single orbit, reconstruction using data from a year in a superposed epoch fashion, the effect of counting noise on the reconstruction, and the effect of using an image denoising technique, called total variation minimization as a regularizer. We found that reconstruction of the 3D X-ray emissions from the magnetosheath is possible with as few as 10 images distributed over a single orbit of SMILE, using nominal regularization. However, using superposed epoch reconstruction with images distributed over an entire year, for similar solar wind conditions and dipole tilt result in a much better reconstruction. Some artifacts appear in some of the reconstructions, which is a common feature of tomographic reconstruction. In the future we will explore reconstruction more broadly using ART-like methods and for a wider range of conditions and noise levels. We will also explore the feasibility of reconstructions with multiple spacecraft.

References

Akasofu, S.-I. (1964), The development of the auroral substorm, *Planetary and Space Science*, *12*(4), 273–282.

Aso, T., M. Ejiri, A. Urashima, H. Miyaoka, Å. Steen, U. Brändström, and B. Gustavsson (1998), First results of auroral tomography from alis-japan multi-station observations in march, 1995, *Earth, planets and space*, *50*(1), 81–86.

Branduardi-Raymont, G., C. Wang, C. Escoubet, M. Adamovic, D. Agnolon, M. Berthomier, J. Carter, W. Chen, L. Colangeli, M. Collier, H. Connor, L. Dai, A. Dimmock, O. Djazovski, E. Donovan, J. Eastwood, G. Enno, F. Giannini, L. Huang, D. Kataria, K. Kuntz, H. Laakso, J. Li, L. Li, T. Lui, J. Loicq, A. Masson, J. Manuel, A. Parmar, T. Piekutowski, A. Read, A. Samsonov, S. Sembay, W. Raab, C. Ruciman, J. Shi, D. Sibeck, E. Spanswick, T. Sun, K. Symonds, J. Tong, B. Walsh, F. Wei, D. Zhao, J. Zheng, X. Zhu, and Z. Zhu (2018), Smile solar wind magnetosphere ionosphere link explorer. definition study report.

Brittnacher, M., J. Spann, G. Parks, and G. Germany (1997), Auroral observations by the polar ultraviolet imager (uvi), *Advances in Space Research*, *20*(4-5), 1037–1042.

C: son Brandt, P., R. Demajistre, E. Roelof, S. Ohtani, D. Mitchell, and S. Mende (2002), Image/high-energy energetic neutral atom: Global energetic neutral atom imaging of the plasma sheet and ring current during substorms, *Journal of Geophysical Research: Space Physics*, *107*(A12), SMP–21.

Chambolle, A. (2004), An algorithm for total variation minimization and applications, *Journal of Mathematical imaging and vision*, *20*(1-2), 89–97.

Collier, M. R., and H. K. Connor (2018), Magnetopause surface reconstruction from tangent vector observations, *Journal of Geophysical Research: Space Physics*, *123*(12), 10–189.

Cravens, T. (1997), Comet hyakutake x-ray source: Charge transfer of solar wind heavy ions, *Geophysical Research Letters*, *24*(1), 105–108.

Cravens, T. E. (2000), Heliospheric x-ray emission associated with charge transfer of the solar wind with interstellar neutrals, *The Astrophysical Journal Letters*, *532*(2), L153.

Gordon, R., R. Bender, and G. T. Herman (1970), Algebraic reconstruction techniques (art) for three-dimensional electron microscopy and x-ray photography, *Journal of theoretical Biology*, *29*(3), 471–481.

Gustavsson, B. (1998), Tomographic inversion for alis noise and resolution, *Journal of Geophysical Research: Space Physics*, *103*(A11), 26,621–26,632.

He, H., C. Shen, H. Wang, X. Zhang, B. Chen, J. Yan, Y. Zou, A. M. Jorgensen, F. He, Y. Yan, et al. (2016), Response of plasmaspheric configuration to substorms revealed by changâĂŹe 3, *Scientific reports*, *6*, 32,362.

Henderson, M., G. Reeves, H. E. Spence, R. Sheldon, A. Jorgensen, J. Blake, and J. Fennell (1997), First energetic neutral atom images from polar, *Geophysical research letters*,

24(10), 1167–1170.

Henderson, M., G. Reeves, K. Moore, H. E. Spence, A. Jorgensen, J. Fennell, J. Blake, and E. Roelof (1999), Energetic neutral atom imaging with the polar ceppad/ips instrument: Initial forward modeling results, *Physics and Chemistry of the Earth, Part C: Solar, Terrestrial & Planetary Science*, *24*(1-3), 203–208.

Hu, Y., X. Guo, and C. Wang (2007), On the ionospheric and reconnection potentials of the earth: Results from global mhd simulations, *Journal of Geophysical Research: Space Physics*, *112*(A7).

Jorgensen, A., L. Kepko, M. Henderson, H. E. Spence, G. Reeves, J. Sigwarth, and L. Frank (2000), Association of energetic neutral atom bursts and magnetospheric substorms, *Journal of Geophysical Research: Space Physics*, *105*(A8), 18,753–18,763.

Jorgensen, A. M., T. Sun, C. Wang, L. Dai, S. Sembay, F. Wei, Y. Guo, and R. Xu (2019a), Boundary detection in three dimensions with application to the smile mission: The effect of photon noise, *Journal of Geophysical Research: Space Physics*, *124*(6), 4365–4383.

Jorgensen, A. M., T. Sun, C. Wang, L. Dai, S. Sembay, J. Zheng, and X. Yu (2019b), Boundary detection in three dimensions with application to the smile mission: the effect of model-fitting noise, *Journal of Geophysical Research: Space Physics*, *124*(6), 4341–4355.

Roelof, E., D. Mitchell, and D. Williams (1985), Energetic neutral atoms (e 50 kev) from the ring current: Imp 7/8 and isee 1, *Journal of Geophysical Research: Space Physics*, *90*(A11), 10,991–11,008.

Rudin, L. I., S. Osher, and E. Fatemi (1992), Nonlinear total variation based noise removal algorithms, *Physica D: nonlinear phenomena*, *60*(1-4), 259–268.

Sandel, B. R., R. A. King, W. Forrester, D. L. Gallagher, A. L. Broadfoot, and C. Curtis (2001), Initial results from the image extreme ultraviolet imager, *Geophysical research letters*, *28*(8), 1439–1442.

Størmer, C. (1935), Measurements of luminous night clouds in norway 1933 and 1934. with 3 figures in the text and 17 plates, *Astrophysica Norvegica*, *1*, 87.

Sun, T., C. Wang, H. K. Connor, A. M. Jorgensen, and S. Sembay (), Deriving the magnetopause position from the soft x-ray image by using the tangent fitting approach, *Journal of Geophysical Research: Space Physics*, p. e2020JA028169.

Sun, T., C. Wang, F. Wei, and S. Sembay (2015), X-ray imaging of kelvin-helmholtz waves at the magnetopause, *Journal of Geophysical Research: Space Physics*, *120*(1), 266–275.

Sun, T., C. Wang, S. Sembay, R. Lopez, C. Escoubet, G. Branduardi-Raymont, J. Zheng, X. Yu, X. Guo, L. Dai, et al. (2019), Soft x-ray imaging of the magnetosheath and cusps under different solar wind conditions: Mhd simulations, *Journal of Geophysical Research: Space Physics*, *124*(4), 2435–2450.

Sun, T., X. Wang, and C. Wang (2021), Tangent directions of the cusp boundary derived from the simulated soft x-ray image, *Journal of Geophysical Research: Space Physics*, *126*(3), e2020JA028,314.

Vallat, C., I. Dandouras, P. C: son Brandt, R. DeMajistre, D. G. Mitchell, E. C. Roelof, H. Rème, J.-A. Sauvaud, L. Kistler, C. Mouikis, et al. (2004), First comparisons of local ion measurements in the inner magnetosphere with energetic neutral atom magnetospheric image inversions: Cluster-cis and image-hena observations, *Journal of Geophysical Research: Space Physics*, *109*(A4).

Wang, C., Z. J. Li, T. R. Sun, Z. Q. Liu, J. Liu, Q. Wu, and et al. (2017), Smile satellite mission survey, *Space International (in Chinese)*, *464*, 13âĂŞ16.

Acknowledgments

This study is supported by the National Natural Science Foundation of China grants (41904148 and 41731070). The model-generated data used for this paper as well as a IDL-language program for reading the data area available at `osf.io/rm3uc/`. For more information about the SMILE mission the reader is referred to `https://sci.esa.int/web/smile/-/61194-smile-definition-study-report-red-book`.

Figure 1.

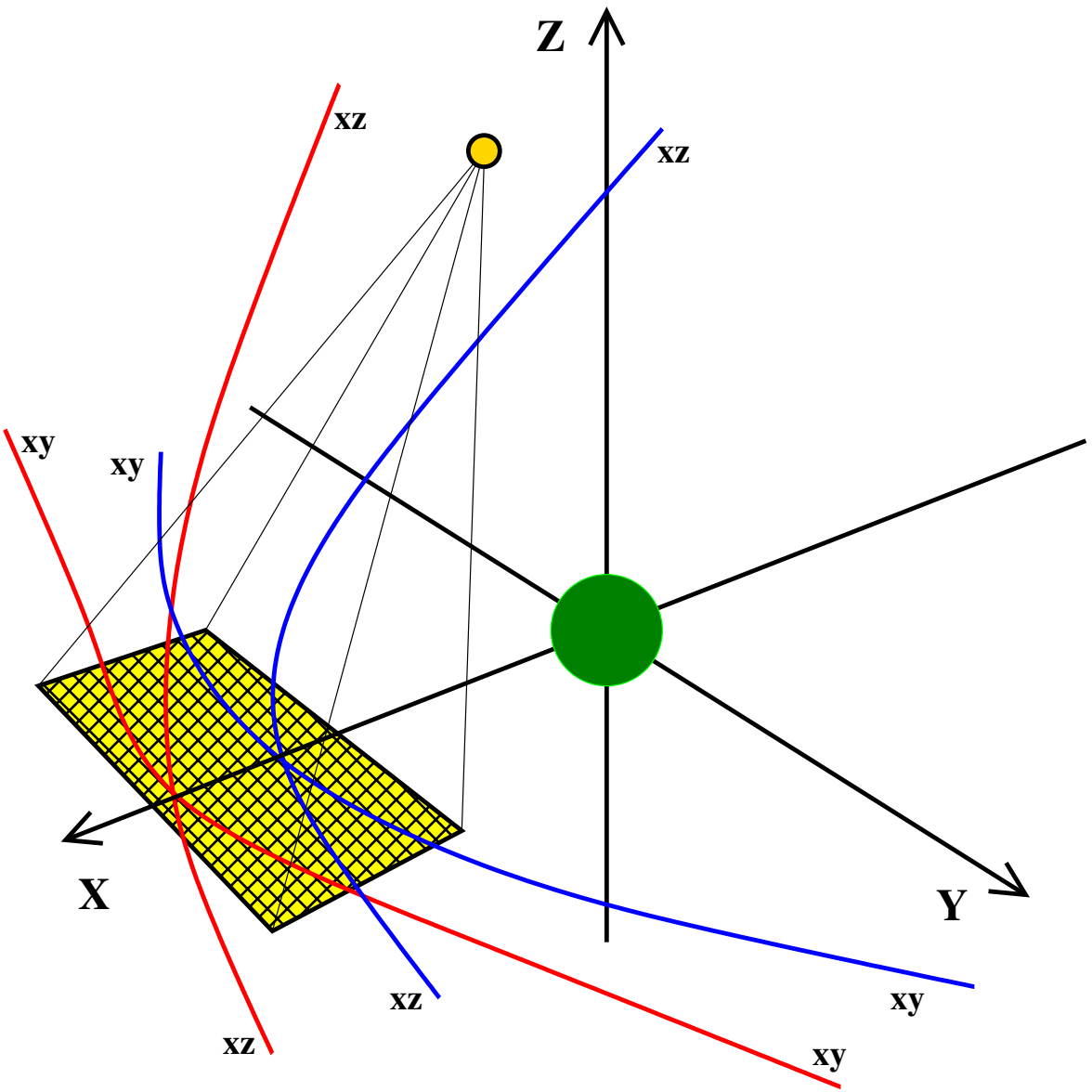
Z
xz
xz
xy
xy
X
Y
xz
xz
xy
xy

Figure 2.

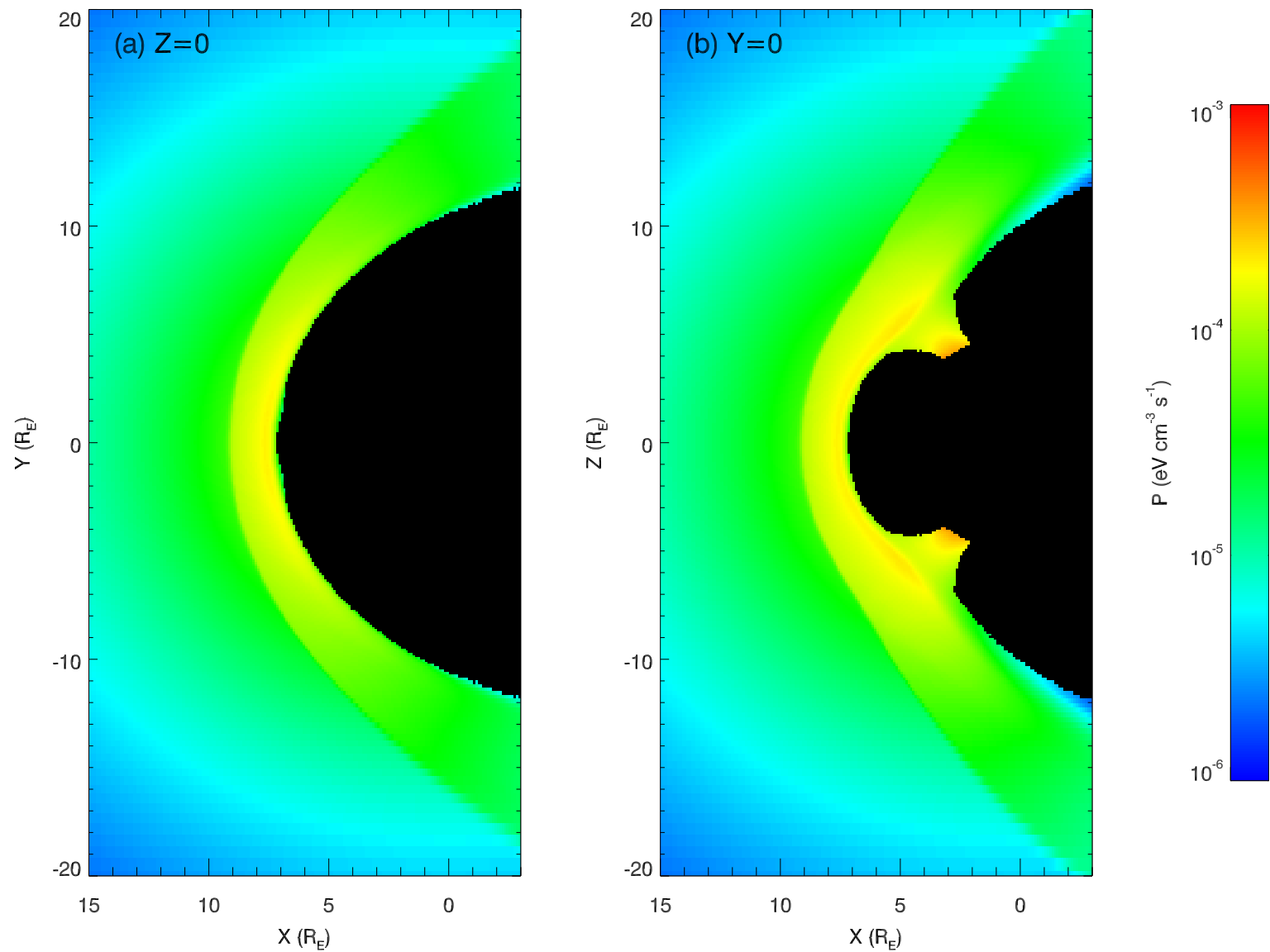
(a) Z=0
(b) Y=0
20
10
0
-10
-20
Y (R_E)
Z (R_E)
15
10
5
0
X (R_E)
P (eV cm^-3 s^-1)
10^-3
10^-4
10^-5
10^-6

Figure 3.

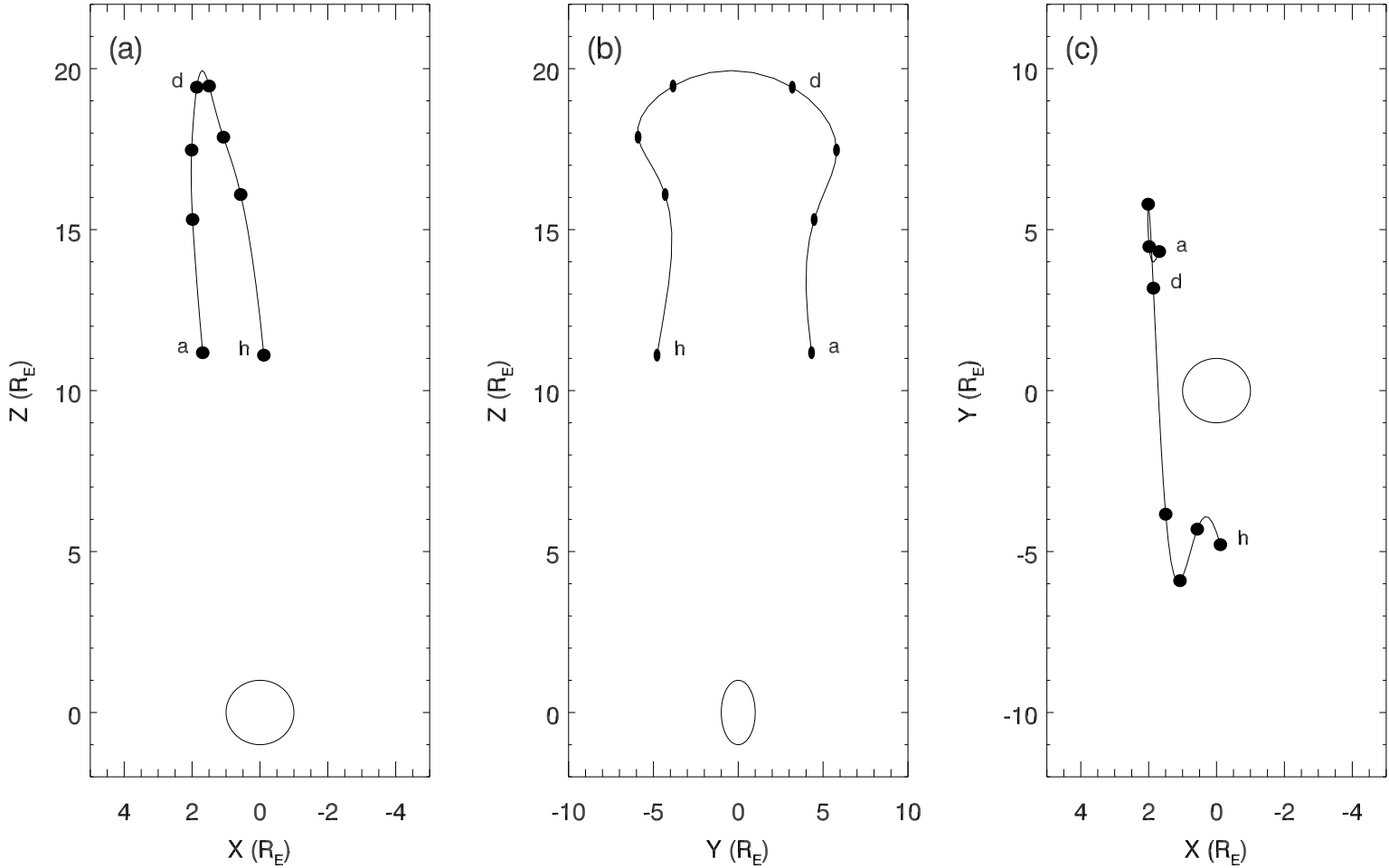
(a)
d
a
h
20
15
10
5
0
Z (R_E)
4
2
0
-2
-4
X (R_E)
(b)
d
h
a
20
15
10
5
0
Z (R_E)
-10
-5
0
5
10
Y (R_E)
(c)
a
d
h
10
5
0
-5
-10
Y (R_E)
4
2
0
-2
-4
X (R_E)

Figure 4.

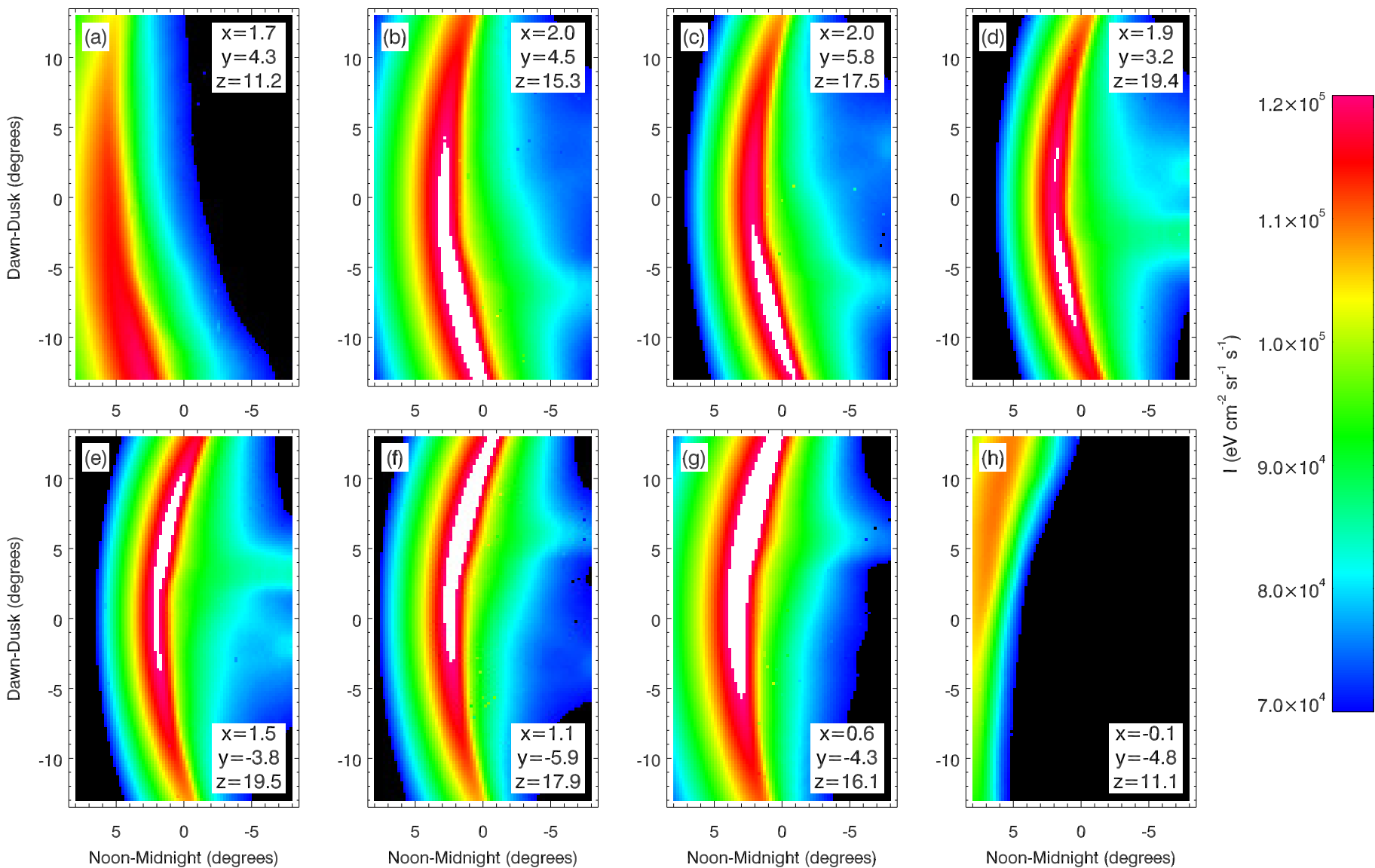
(a)
x=1.7
y=4.3
z=11.2
(b)
x=2.0
y=4.5
z=15.3
(c)
x=2.0
y=5.8
z=17.5
(d)
x=1.9
y=3.2
z=19.4
(e)
x=1.5
y=-3.8
z=19.5
(f)
x=1.1
y=-5.9
z=17.9
(g)
x=0.6
y=-4.3
z=16.1
(h)
x=-0.1
y=-4.8
z=11.1
Dawn-Dusk (degrees)
Noon-Midnight (degrees)
I (eV cm^{-2} sr^{-1} s^{-1})
1.2×10^5
1.1×10^5
1.0×10^5
9.0×10^4
8.0×10^4
7.0×10^4

Figure 5.

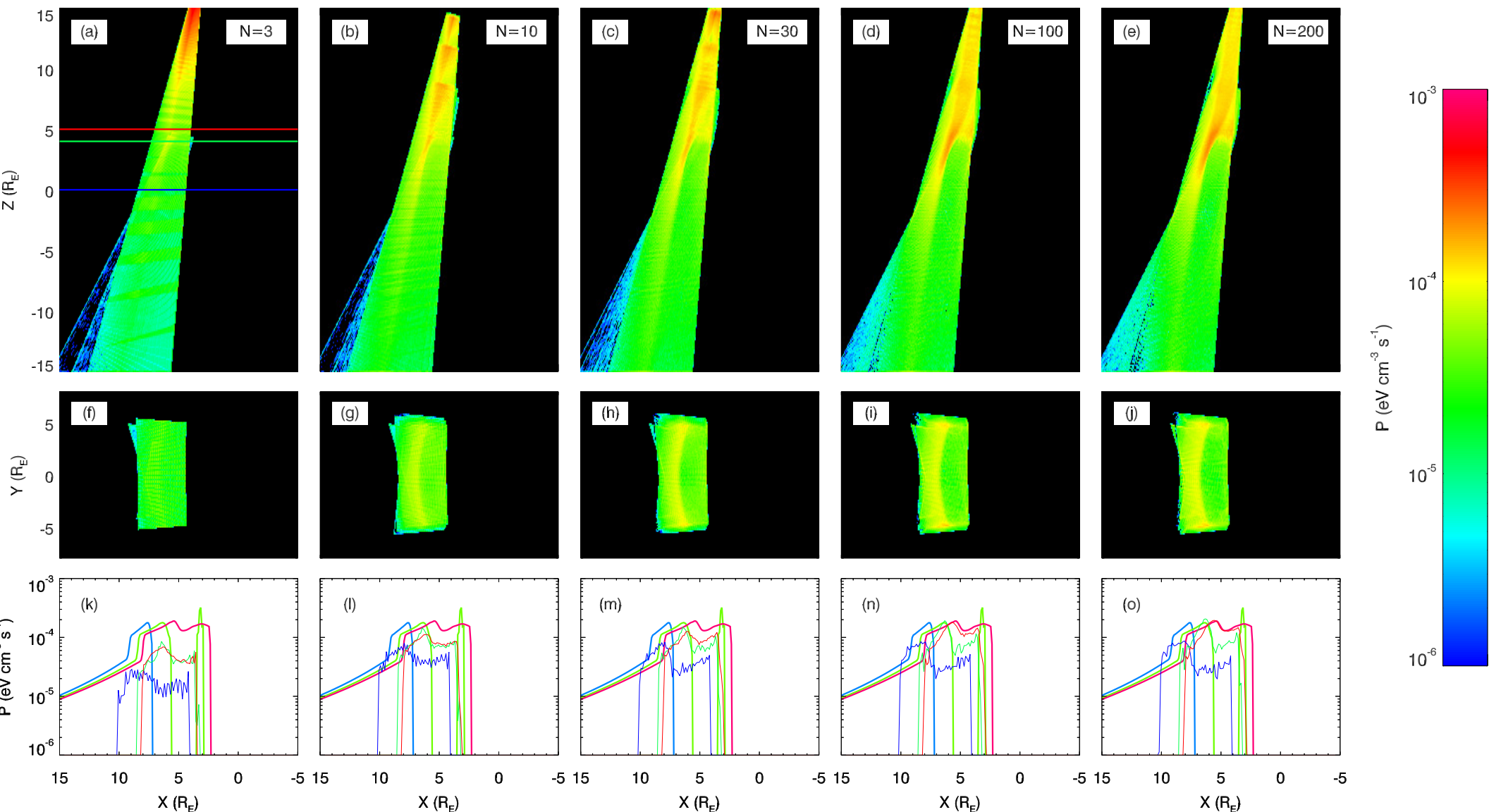
(a)
N=3
(b)
N=10
(c)
N=30
(d)
N=100
(e)
N=200
Z (R_E)
(f)
(g)
(h)
(i)
(j)
Y (R_E)
(k)
(l)
(m)
(n)
(o)
P (eV cm^-3 s^-1)
X (R_E)
15
10
5
0
-5
-10
-15
10^-3
10^-4
10^-5
10^-6

Figure 6.

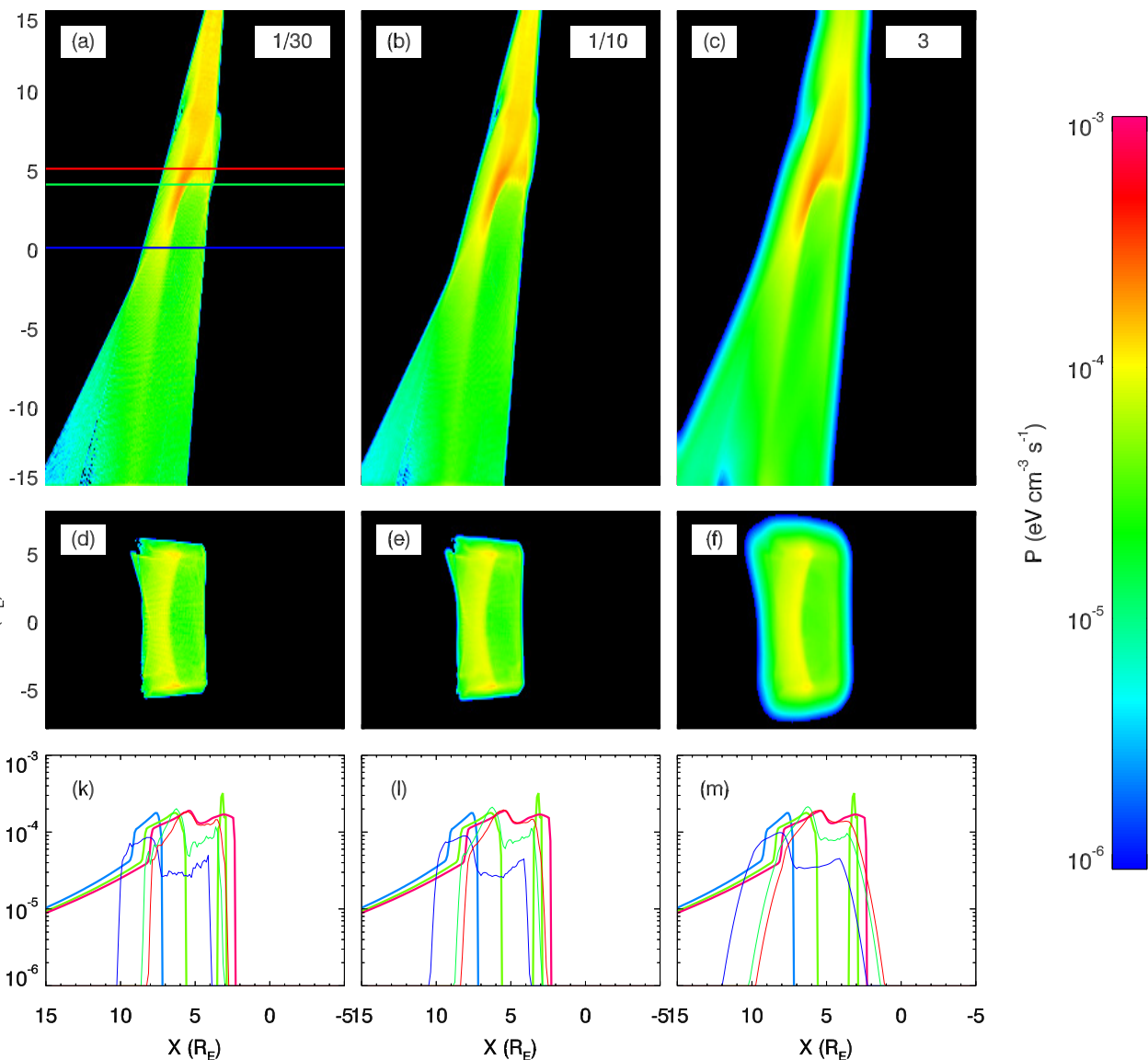
(a)
1/30
(b)
1/10
(c)
3
(d)
(e)
(f)
(k)
(l)
(m)
15
10
5
0
-5
-10
-15
10^{-3}
10^{-4}
10^{-5}
10^{-6}
X (R_E)
P (eV cm^{-3} s^{-1})

Figure 7.

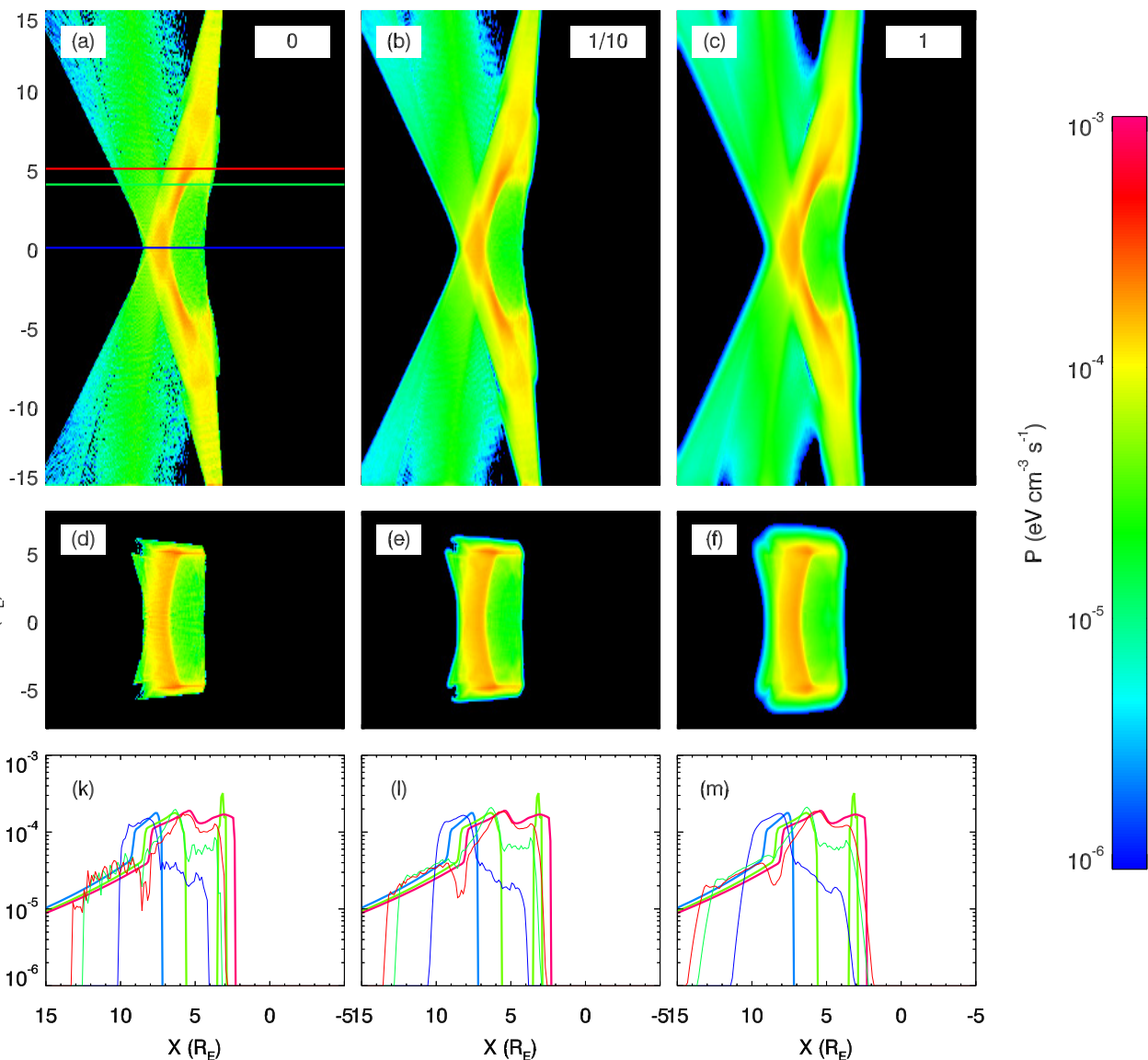
(a)
0
(b)
1/10
(c)
1
(d)
(e)
(f)
(k)
(l)
(m)
15
10
5
0
-5
-10
-15
10^{-3}
10^{-4}
10^{-5}
10^{-6}
X (R_E)
P (eV cm^{-3} s^{-1})

Figure 8.

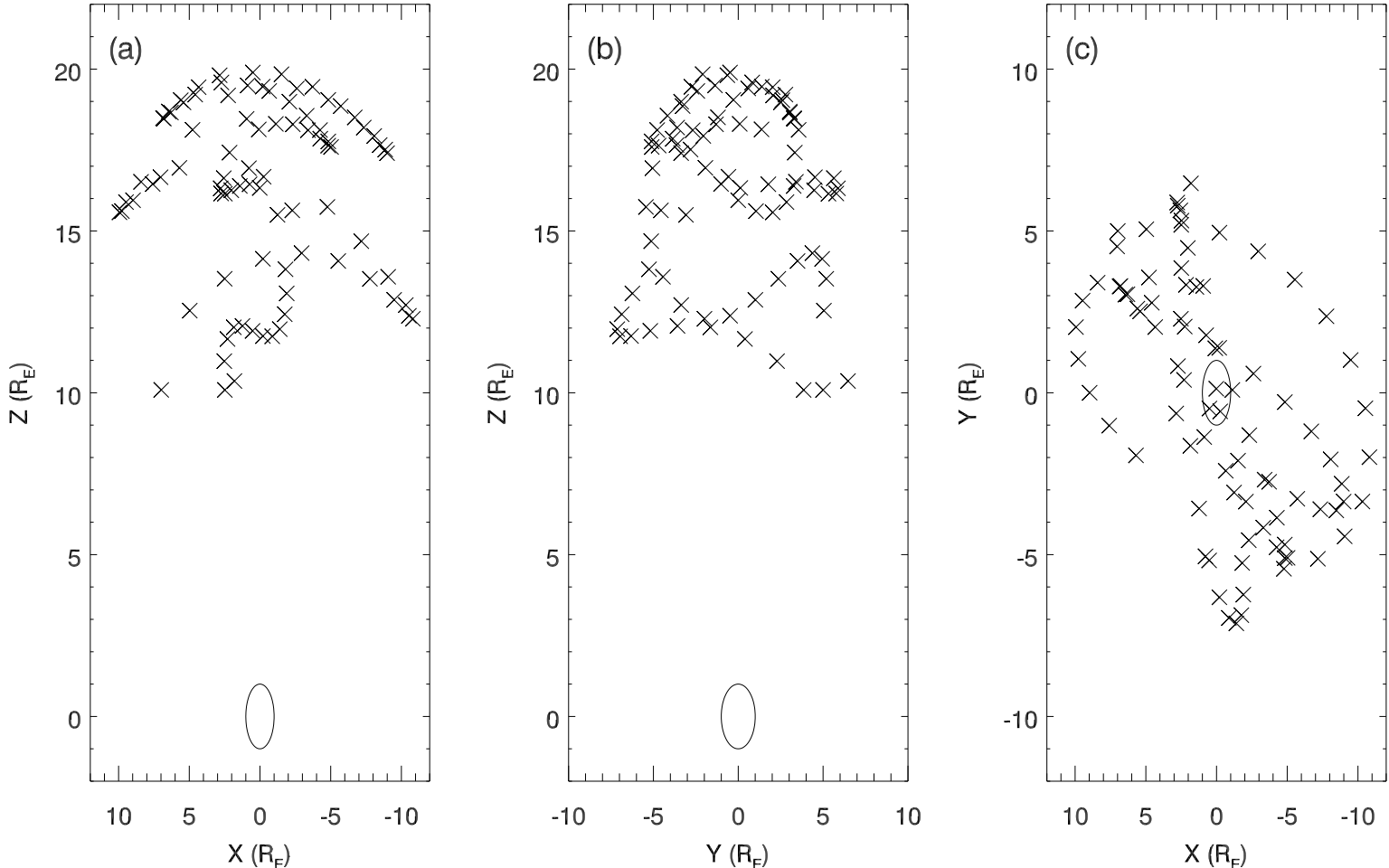
(a)
(b)
(c)
Z (R_E)
Y (R_E)
X (R_E)
20
15
10
5
0
-5
-10

Figure 9.

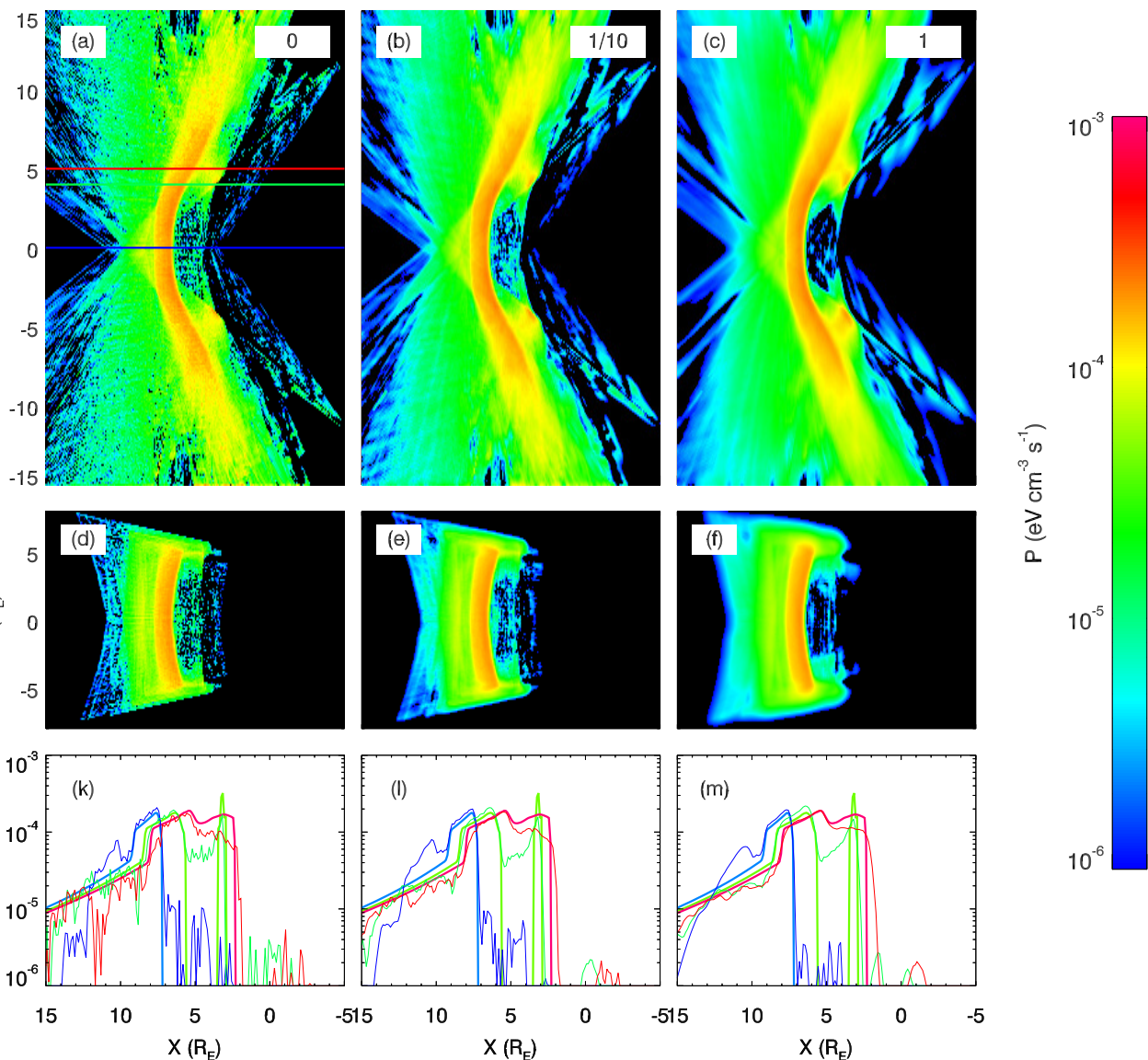
(a)
0
(b)
1/10
(c)
1
(d)
(e)
(f)
(k)
(l)
(m)
15
10
5
0
-5
-10
-15
10^{-3}
10^{-4}
10^{-5}
10^{-6}
X (R_E)
P (eV cm^{-3} s^{-1})

Figure 10.

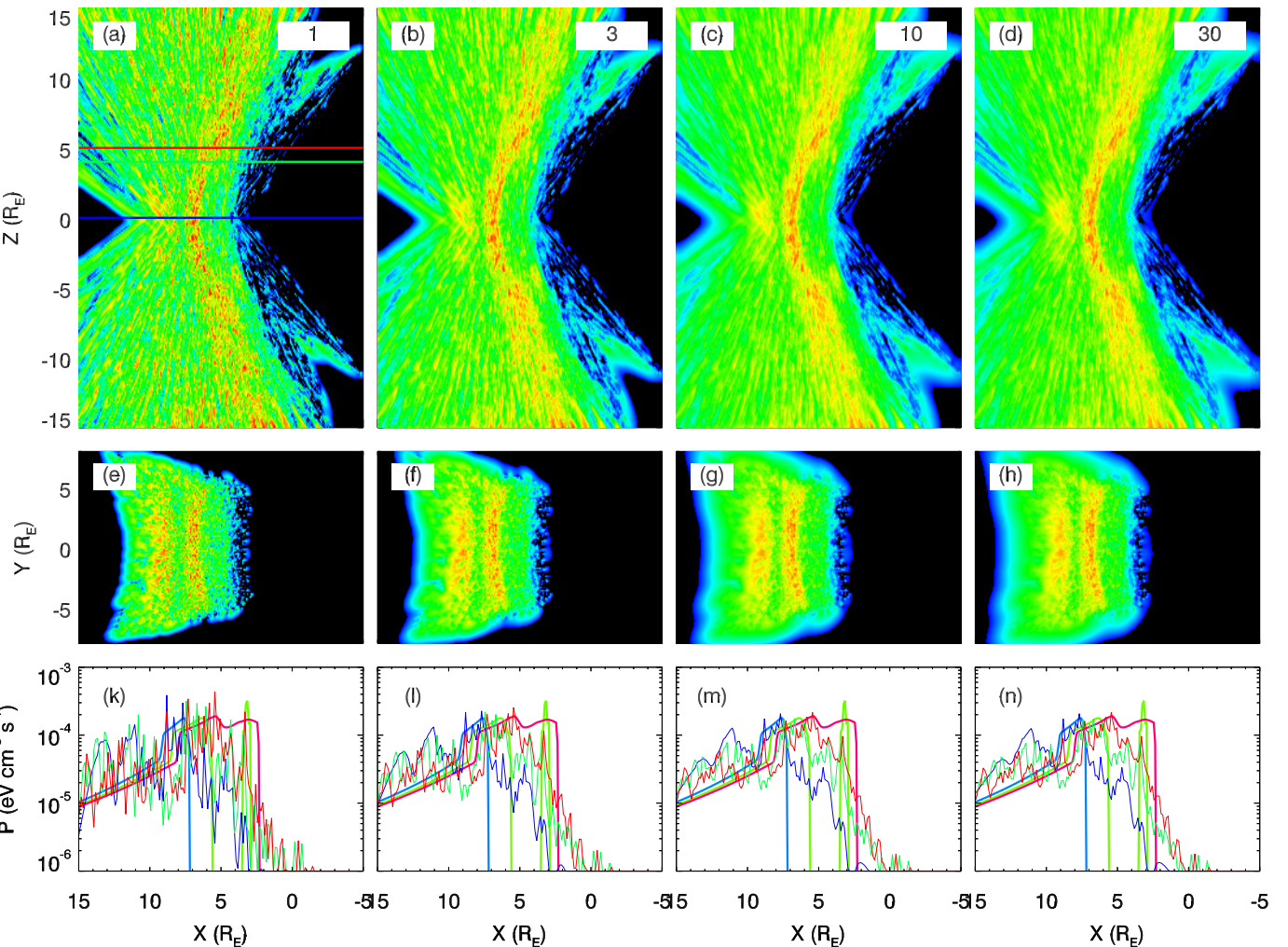
(a)
1
(b)
3
(c)
10
(d)
30
(e)
(f)
(g)
(h)
(k)
(l)
(m)
(n)
Z (R_E)
Y (R_E)
P (eV cm^-3 s^-1)
X (R_E)
15
10
5
0
-5
-15
10^-3
10^-4
10^-5
10^-6